

~~RESTRICTED~~Copy  
RM E9E06

NACA RM E9E06

UNCLASSIFIED



# RESEARCH MEMORANDUM

ANALYSIS AND PRELIMINARY INVESTIGATION OF EDDY-CURRENT HEATING  
FOR ICING PROTECTION OF AXIAL-FLOW-COMPRESSOR BLADES

By Thomas Dallas and C. Ellisman

Lewis Flight Propulsion Laboratory  
Cleveland, Ohio

**CLASSIFICATION CANCELLED**

Authority J. W. Crawley Date 12/14/53  
2010501  
By J. H. 1/4/54 See WACA  
CLASSIFIED DOC. REF 1908

This document contains classified information affecting the National Defense of the United States within the meaning of the Espionage Act, USC 6023 and 32. Its transmission or the revelation of its contents in any manner to an unauthorized person is prohibited by law. Information so classified may be imported only to persons in the military and naval services of the United States, appropriate civilian officers and employees of the Federal Government who have a legitimate interest therein, and to United States citizens of known loyalty and discretion who of necessity must be informed thereof.

## NATIONAL ADVISORY COMMITTEE FOR AERONAUTICS

WASHINGTON

UNCLASSIFIED

August 8, 1949

~~RESTRICTED~~

A. A. A. LIBRARY

U.S. AIR FORCE RESEARCH AND DEVELOPMENT  
H. J. 1949



UNCLASSIFIED

## NATIONAL ADVISORY COMMITTEE FOR AERONAUTICS

RESEARCH MEMORANDUMANALYSIS AND PRELIMINARY INVESTIGATION OF EDDY-CURRENT HEATING  
FOR ICING PROTECTION OF AXIAL-FLOW-COMPRESSOR BLADES

By Thomas Dallas and C. Ellisman

## SUMMARY

An analysis and a preliminary experimental investigation of the use of eddy currents for heating the blades of an axial-flow compressor of a turbojet engine as a means of ice protection is presented. Steinmetz's analysis of eddy currents in flat plates is extended and formulas are derived that permit calculations of currents, voltages, flux distribution, and power when operation is not limited to conditions of constant permeability.

The application of eddy-current heating appears to be feasible for the generation of power densities required for icing protection of axial-flow-compressor blades.

## INTRODUCTION

The advent of all-weather flying of jet-propelled aircraft demands provision for complete ice protection of the engines. One component of this type of engine that has not been provided with ice protection is the compressor inlet, although NACA flight investigations of an axial-flow-compressor-type turbojet engine have indicated that the compressor inlet is subject to icing.

Three methods have been proposed by the NACA to protect the engine: (1) Inertia separation of the water droplets from the induction air (reference 1); (2) heating of the charge air (reference 2); and (3) heating of the engine parts by hot gas (by a method similar to that of reference 3). A fourth method of de-icing, which involves heating of the engine parts by the use of electrical eddy currents that can be induced if a pulsating magnetic field is created in the blades to be protected, is proposed by the NACA Lewis laboratory and discussed herein.

An analysis of eddy currents in a compressor blade, the geometry of which has been limited to that of a flat plate for

~~RESTRICTED~~ UNCLASSIFIED

simplicity, is presented. Formulas are derived that permit calculations of currents, voltages, flux distribution, and power when operation is not limited to conditions of constant permeability. Preliminary investigations are described in which a model blade is subjected to flux variations and the heat generated is determined as a function of magnetizing ampere turns. The heat required for adequate protection of the inlet guide vanes is estimated. Conclusions based on experiment and theory are stated regarding the suitability of the method, and statements are included regarding the significant parameters.

#### DESCRIPTION OF EDDY-CURRENT HEATING

The configuration of a typical axial-flow compressor (fig. 1) lends itself to a design that incorporates an eddy-current generator. The principle of eddy-current heating as applied to the inlet guide vanes is illustrated by the schematic diagram of figure 2. In order to apply eddy-current heating, the blading involved must be of ferromagnetic material. In addition, a ferromagnetic flux path must be provided to complete the magnetic circuit. A direct-current coil is needed to supply magnetomotive force required for operation of the system. A flux-chopping mechanism (section A-A, fig. 2) provides a varying air gap. The varying reluctance of the air gap causes a flux change, which results in the creation of eddy currents and heat.

It will subsequently be shown that it is desirable to use flux variations of high frequency. In a typical axial-flow compressor having 88 inlet guide vanes and operating at 7600 rpm, a cursory examination (without investigation of all design criterions) indicates that 44 chopper teeth could be used to give a frequency of 5600 cycles per second. At this frequency, any appreciable flux variation in parts of the magnetic circuit other than the blading would cause undesired heating and loss of energy. In addition, if flux variation in parts other than the blading is allowed, the time constants of the coil and other parts involved may make it impossible to obtain the full amplitude of flux variation in the blades at the frequencies under consideration and the system may fail to operate. (Because it is impossible to maintain constant flux in all parts of the chopper, lamination of the chopper will minimize the difficulties discussed.)

The foregoing principles dictate a design criterion typically illustrated in section A-A of figure 2. The teeth in the chopper should be of such a length that as one blade is leaving a tooth another blade is taking its place in the magnetic circuit. In this

manner, the only parts of the magnetic circuit that are experiencing a flux change are the blading and the immediately adjacent parts. A constant flux is thus maintained in the rest of the magnetic circuit and a constant flux always links the coil.

In a general application of eddy-current heating where more than one set of blades is protected, the chopper may be either in the rotor or the stator but the blades to be heated must pass over the teeth of the chopper. A chopper must therefore be provided for each row of blades to be protected.

In compressor-blade heating by means of eddy currents, flux in the blades can be either unidirectional-pulsating or alternating. In the following analysis, however, only the alternating-flux case is considered. An experimental correlation between this type of operation and the unidirectional-pulsating type is presented.

#### SYMBOLS

The following symbols are used in this report:

A	cross-sectional area of blade, square centimeters
$B_{max}$	maximum value of alternating flux density, gaussses
$B_{max u}$	maximum value of alternating flux density under uniform-flux distribution, gaussses
c	constant, $\sqrt{0.4 \pi^2 f \gamma \mu 10^{-8}}$ , centimeters <sup>-1</sup>
d	plate thickness, centimeters
E	root-mean-square value corresponding to $E_{max}$ , volts per centimeter
$E_{max}$	maximum value of alternating voltage gradient (in direction of plate width), volts per centimeter
f	frequency, cycles per second
$H_{max}$	maximum value of alternating-magnetic-field intensity (in direction of plate length), oersteds
I	root-mean-square value corresponding to $I_{max}$ , amperes per centimeter

$I_{\max}$	maximum value of alternating current per centimeter length of plate; equilibrant of all currents in incremental volumes included from plate center to any plane parallel to outer plate surface, amperes per centimeter
$j$	complex operator equivalent to $\sqrt{-1}$
$L$	length of blade, centimeters
$l$	distance from plane ABC (fig. 3) toward outer surface of plate, centimeters
$l_o$	one-half of plate thickness $d$ , centimeters
$l_p$	depth of penetration at constant permeability $\mu$ , centimeters
$l_{p \text{ av}}$	depth of penetration at average permeability $\mu_{\text{av}}$ , centimeters
$l_T$	total depth of penetration $l_{p1} + l_{p2}$ , centimeters
$l_2$	upper limit of $l$ for given impressed field intensity of $H_{\max 2}$ , centimeters
$NI$	total root-mean-square ampere turns
$N_{aI_{\max a}}$	maximum value of alternating ampere turns required across air gap
$N_{bI_{\max b}}$	maximum value of alternating ampere turns required across blade
$P_T$	total air-gap permeance, centimeters
$P_1 \dots P_8$	permeances of various volumes composing air gaps, centimeters
$p$	eddy-current power generated for uniform flux distribution, watts
$p_e$	eddy-current power generated per square centimeter of blade surface, watts per square centimeter
$p_e'$	eddy-current power generated per square inch of blade surface, watts per square inch

$s$	distance from surface ABC (fig. 3) toward center of plate, centimeters
$V$	plate volume, cubic centimeters
$\alpha$	mean of $\beta$ - $\delta$ (fig. 6), degrees
$\alpha_2$	limiting value of $\alpha$ , mean of $\beta_2$ - $\delta_2$ , degrees
$\beta$	angle between $I_{\max 1}$ and $I_{\max}$ (fig. 6), degrees
$\beta_2$	upper limit of $\beta$ , angle between $I_{\max 1}$ and $I_{\max 2}$ , degrees
$\gamma$	conductivity, mhos per centimeter
$\delta$	angle between $\Phi_{\max 1}$ and $\Phi_{\max}$ (fig. 6), degrees
$\delta_2$	upper limit of $\delta$ , angle between $\Phi_{\max 1}$ and $\Phi_{\max 2}$ , degrees
$\theta$	power-factor angle (fig. 5), degrees
$\mu$	constant magnetic permeability, $(B_{\max 1}/H_{\max 1})$
$\mu_{av}$	average magnetic permeability
$\rho$	resistivity, $(1/\gamma)$ , ohm-centimeters
$\Phi_{\max}$	maximum value of alternating flux included in cross-sectional area having width of 1 centimeter and thickness with limits from plate center line to an outer limit, which is plane where field intensity is $H_{\max}$ , maxwells

## Subscripts:

$s$	values in or to plane ABC of plate (fig. 3)
1	values in or to plane ABC (fig. 3) when field intensity at plane ABC has reached value at saturation point $H_{\max 1}$ on magnetization curve
2	upper limiting values where field intensity is given impressed field intensity $H_{\max 2}$ and flux density is saturation value $B_{\max 1}$

Overscoring indicates vector quantities.

## ANALYSIS

## Development of Analysis

In eddy-current calculations for plates, the following formula is commonly used for determining power when a sine wave of alternating flux at frequency  $f$  is employed:

$$p = \frac{\pi^2 d^2 \gamma f^2 (B_{\max} u)^2 V}{6} 10^{-16} \text{ watts} \quad (1)$$

This expression is valid if the magnetic effect of eddy currents is negligible and if the lines of force are uniformly distributed throughout the plate and are parallel to the sides of the plate.

Eddy currents, by virtue of their countermagnetomotive force, tend to damp the flux in the center of the cross section of the magnetic material. The depth of penetration of the flux into the surface of a plate of magnetic material is given by Steinmetz (reference 4, p. 371) as

$$l_p \text{ av} = \frac{3570}{\sqrt{\gamma \mu_{\text{av}} f}} \quad (2)$$

At a frequency of 6100 cycles per second, for instance, an assumed average permeability of 119, and a conductivity of  $10^5$  mho-centimeters corresponding to soft iron, the penetration would be 0.0132 centimeter or 0.0052 inch. With an average blade thickness of approximately 0.062 inch, it is apparent that because of the damping action, the flux density is negligible throughout the greatest portion of the blade cross section and that a serious error is involved in considering it otherwise.

Steinmetz (reference 4) has considered alternating-magnetic-flux distribution only under conditions of constant permeability. In the present work, however, operation well past the knee of the magnetization curve is necessary and the work of Steinmetz is not directly applicable. Steinmetz considered a section of a flat plate or lamination similar to that shown in figure 3. He divided the plate into incremental slices of width  $ds$  at distance  $s$  from the surface of the plate and set up the partial differential equations of the system. The direction of the flux was assumed along the length or longest dimension of the plate.

Steinmetz found that, if the flux at the center of the plate is negligible, the maximum flux density  $\bar{B}_{\max}$  at any point at depth  $s$  from the plate surface is given by

$$\bar{B}_{\max} = B_{\max} s e^{-cs} (\cos cs - j \sin cs) \quad (3)$$

An examination of equation (3) reveals the nature of flux penetration into the surface of the plate. At the surface of the plate, or when  $s = 0$ ,  $\bar{B}_{\max}$  is equal to  $B_{\max} s$ , which is the flux density produced by the impressed magnetomotive force. The real part of equation (3) is therefore in time phase with the impressed magnetomotive force. It is apparent that the flux lags in time and decreases rapidly in value with depth  $s$  into the plate. At a depth equivalent to  $cs$  equal to  $\pi/2$ , the flux lags  $90^\circ$  and is decreased to 20 percent of its value at the surface. When  $cs$  is equal to  $\pi$ , the flux lags  $180^\circ$  but its intensity is only 5 percent. At the point where the flux is again in phase with the impressed magnetomotive force, its value is only 0.2 percent.

Integration of equation (3) between the limits  $s = 0$  and  $s = l_0$  produces the maximum flux in one-half of the plate for 1 centimeter of width. The condition that the flux in the center of the plate is zero dictates that  $e^{-cl_0}$  is negligible; therefore

$$\bar{\Phi}_{\max s} = \frac{B_{\max} s}{2c} (1-j) \quad (4)$$

or

$$\left| \bar{\Phi}_{\max s} \right| = \frac{B_{\max} s}{\sqrt{2} c} \quad (4a)$$

Equation (4) may be used to obtain the mean maximum flux density  $\bar{B}_{\max m}$  by dividing by  $l_0$ :

$$\bar{B}_{\max m} = \frac{\bar{\Phi}_{\max s}}{l_0} = \frac{B_{\max} s}{2cl_0} (1-j) \quad (5)$$

If  $B_{\max m}$  is made equal to  $B_{\max s}$ , then  $l_0$  becomes the depth of penetration  $l_p$  or is the depth to which the flux would penetrate to produce the same total flux if the flux density at the surface was maintained throughout the section of the plate.



$$\bar{l}_p = \frac{1}{2c} (1-j) \quad (6)$$

or

$$\left| l_p \right| = \frac{1}{\sqrt{2} c} \quad (7)$$

Inasmuch as Steinmetz's work is not directly applicable because of operation past the knee of the magnetization curve, further development is necessary. Consideration will still be limited to the flat plate of figure 3. No generality will be lost by this limitation on shape, however, because effects of eddy currents will be shown to be independent of plate thickness  $d$  and to be functions of the surface only (provided flux density at the center of the object is negligible).

A brief general statement will establish the concept of the analysis. Until saturation is reached, the absolute value of the maximum flux density  $B_{\max s}$  in the outer surface increases with impressed magnetomotive force and decreases in absolute value exponentially with distance into the material according to equation (3). As the impressed magnetomotive force is increased beyond saturation, the maximum flux density in the outer surface cannot increase further, but a different action results. The absolute value of the flux density remains essentially constant for a short distance into the plate before decreasing exponentially. The distance of this penetration at constant flux density is determined by the amount of impressed magnetomotive force in excess of that required for saturation.

The normal magnetization curve for SAE 1020 steel, annealed at 1500° F and furnace-cooled, was chosen as a representative curve for purposes of analysis. The curve, which is plotted in figure 4 from data of reference 5, is a plot of flux density in gaussses as a function of field intensities in oersteds. The magnetization curve is approximated by two straight lines; the line AF drawn from the origin approximately tangent to the curve and another line representing the saturation flux density  $B_{\max 1}$  drawn parallel to the abscissa axis at approximately the mean flux density for a given range of field intensity. The mean is estimated from the geometry of the curve of figure 4. As will subsequently be shown, most of the heat is generated in the outer layers of the plate at the higher magnetomotive forces, which is justification for giving greater weight to the higher flux densities. The choice of the

mean is not critical because  $B_{\max 1}$  enters into the final power formula to the one-half power and a 4-percent error in estimating  $B_{\max 1}$  results in a 2-percent error, approximately, in the power. The lines BC, DE, and FG are for limiting values of field intensity of 6, 30, and 50 oersteds, respectively. In order to make the problem specific, let the limiting maximum field intensity  $H_{\max 2}$  be 30 oersteds; then the curve will be represented by lines AD and DE. It is apparent that Steinmetz's equations are applicable along the line AD where the permeability  $\mu$ , which is the slope of line AD, is constant.

Equations (3) to (7) can be represented by the vector diagram of figure 5. Time phase is measured by counterclockwise rotation. The reference vector  $I_{\max s}$  extends from the pole toward the upper left. The equality of the flux components of equation (4) fixes the current at a lagging power-factor angle of  $45^\circ$  with respect to the impressed voltage. The voltage of self-induction  $E_{\max s}$  lags its flux  $\Phi_{\max s}$  by  $90^\circ$ ; whereas the impressed or consumed voltage, which is equal but opposite to  $E_{\max s}$ , leads by  $90^\circ$ . This diagram can be chosen to represent conditions at the saturation point D of figure 4. Then other points along the line AD, which represent conditions at deeper penetration into the plate, can be represented by vectors having the same relative proportionality and phase, but which are shifted clockwise to the proper lagging time phase relative to conditions at point D and which are reduced in magnitude by the factor  $e^{-cs}$ .

Two more equations are required to establish the magnitudes of the voltages and current in figure 5. The maximum voltage  $E_{\max s}$  of self-induction per centimeter width of plate from the flux  $\Phi_{\max s}$  is

$$E_{\max s} = 2\pi f \Phi_{\max s} 10^{-8} \quad (8)$$

In order to eliminate any turns-ratio numbers, the assumption is made that the impressed magnetomotive force is supplied by a one-turn coil. As previously stated, the flux density  $B_{\max s}$  at the outer surface of the plate is that due to the primary magnetomotive force alone because no effects of bucking eddy currents exist at the surface. Because the flux is assumed to be along straight lines parallel to the sides of the plate, the equation for the intensity of the field at the surface is

$$H_{\max s} = 0.4 \pi I_{\max s} \quad (9)$$

where

$I_{\max}$  s value in SYMBOLS (also, current required in a one-turn energizing coil to furnish a field intensity of  $H_{\max}$  s for volume of plate (fig. 3) 1 cm wide, 1 cm long, and depth equal to one-half plate thickness), amperes per centimeter

The vector diagram of figure 5 represents the flux, the current, and the voltage associated with the volume of the plate described in the preceding symbol definition. With the vector diagram of figure 5 chosen to represent the conditions at the point D of the magnetization curve (fig. 4), the outer surfaces ABC and A'B'C' of figure 3 will be saturated at a flux density  $B_{\max}$  1 under a field intensity of  $H_{\max}$  1. Equations (4a) and (7) now become

$$|\Phi_{\max} 1| = \frac{B_{\max} 1}{\sqrt{2} c} \quad (4b)$$

and

$$|I_p 1| = \frac{1}{\sqrt{2} c} \quad (7a)$$

In the analysis it was found convenient to use the following physical concept. The assumption was made that thin sheets of SAE 1020 steel of incremental thickness  $dl$  are added to the surfaces ABC and A'B'C' and become integral with the original plate of material. In addition, it was assumed that the impressed magnetomotive force is increased to balance the bucking eddy currents in the new sheets in order that the flux densities at planes ABC and A'B'C' remain unchanged. Then the vector diagram of figure 6 will represent the new conditions.

The dashed vectors of figure 6 are a duplication of figure 5, with the exceptions that the flux-component vectors have been omitted for clarity and the vectors now represent conditions at the saturation point. The diagram continues the representation of a plate volume having a surface 1 centimeter square and a depth equal to one-half the plate thickness. Regardless of saturation, it is assumed that currents, voltages, and flux are still representable by vectors and, in the case of figure 6, by maximum values of sine waves. As the new sheets of thickness  $dl$  at constant flux density  $\bar{B}_{\max} 1$  are added, the vectors will change

in absolute value and position, as indicated by the dashed lines representing their loci. It was assumed that sufficient sheets have been added to reach the limiting maximum field intensity  $H_{\max 2}$  of 30 oersteds that was chosen. The various quantities at this condition will be identified by the subscript 2.

When a new sheet is added, the total flux is increased by the vector  $\bar{E}_{\max 1} dl$ , which is in phase with the current  $\bar{I}_{\max}$ , as shown in the diagram (fig. 6). From equation (4b) and with  $B_{\max 1}$  a constant, it is possible to write the equation for the absolute value of the maximum flux  $\bar{\Phi}_{\max}$  from the diagram

$$\Phi_{\max} = \Phi_{\max 1} + \int_0^l B_{\max 1} \cos (45^\circ + \beta - \delta) dl = \frac{B_{\max 1}}{\sqrt{2} c} + B_{\max 1} l \cos (45^\circ + \alpha) \quad (10)$$

where  $\alpha$  is the mean value of  $(\beta - \delta)$  for the given value of  $l$ .

The infinitesimal change in maximum field intensity  $dH_{\max}$  between the sides of a sheet is proportional to the current in the sheet

$$dH_{\max} = 0.4 \pi \gamma E_{\max} dl$$

or

$$\frac{dH_{\max}}{dl} = 0.4 \pi \gamma E_{\max} \quad (11)$$

where  $E_{\max}$  is the maximum voltage per centimeter width induced in the sheet by the included flux  $\Phi_{\max}$ . The relation between  $E_{\max}$  and  $\Phi_{\max}$  is

$$E_{\max} = 2 \pi f \Phi_{\max} 10^{-8} \quad (12)$$

From equations (10), (11), and (12), the following relation is obtained:

$$\frac{dH_{\max}}{dl} = \sqrt{2} \frac{0.4\pi^2 \gamma f B_{\max 1}}{c} \left[ 1 + \sqrt{2} cl \cos(45^\circ + \alpha) \right] 10^{-8} \quad (13)$$

When  $\mu H_{\max 1} = B_{\max 1}$  is substituted and equation (13) is integrated in the limits from 0 to  $l_2$ ,  $H_{\max 1}$  to  $H_{\max 2}$ , the absolute value of the maximum field intensity  $H_{\max 2}$  is

$$H_{\max 2} = H_{\max 1} + \sqrt{2} c H_{\max 1} \left[ l_2 + \sqrt{2} \frac{cl_2^2}{2} \cos(45^\circ + \alpha_2) \right] \quad (14)$$

from which the value of  $l_2$  will be

$$l_2 = - \frac{1}{\sqrt{2} c \cos(45^\circ + \alpha_2)} + \sqrt{\frac{1}{2c^2 \cos^2(45^\circ + \alpha_2)} + \frac{1}{c^2 \cos(45^\circ + \alpha_2)} \left( \frac{H_{\max 2}}{H_{\max 1}} - 1 \right)} \quad (15)$$

or

$$1 + \sqrt{2} cl_2 \cos(45^\circ + \alpha_2) = \sqrt{1 + 2 \cos(45^\circ + \alpha_2) \left( \frac{H_{\max 2}}{H_{\max 1}} - 1 \right)} \quad (15a)$$

Also, squaring both sides,

$$\sqrt{2} cl_2 + c^2 l_2^2 \cos(45^\circ + \alpha_2) = \frac{H_{\max 2}}{H_{\max 1}} - 1 \quad (15b)$$

The total depth of penetration is the sum of equations (15) and (7a)

$$l_T = l_{p1} + l_2 = \frac{1}{c\sqrt{2}} \left\{ 1 + \frac{1}{\cos(45^\circ + \alpha_2)} \left[ 1 + \sqrt{1 + 2 \cos(45^\circ + \alpha_2) \left( \frac{H_{\max 2}}{H_{\max 1}} - 1 \right)} \right] \right\} \quad (15c)$$

The voltage gradient  $E_{\max 2}$  in the outer plate surface can be derived by using equations (10) and (12) and substituting the upper limits  $\Phi_{\max 2}$  for  $\Phi_{\max}$ , and  $l_2$  for  $l$ ,

$$E_{\max 2} = \sqrt{2} \pi f 10^{-8} \frac{B_{\max 1}}{c} \left[ 1 + \sqrt{2} c l_2 \cos (45^\circ + \alpha_2) \right] \quad (16)$$

Substitution of equation (15a) and division by  $\sqrt{2}$  to obtain the effective value  $E_2$  on the assumption of a sine wave, gives

$$E_2 = \pi f 10^{-8} \frac{B_{\max 1}}{c} \sqrt{1 + 2 \cos (45^\circ + \alpha_2) \left( \frac{H_{\max 2}}{H_{\max 1}} - 1 \right)} \quad (16a)$$

where

$E_2$  value in SYMBOLS (also the root-mean-square value of impressed voltage required for plate volume having surface 1 cm square and depth equal to one-half plate thickness), volts per centimeter

The relation of equation (15a) may now be used to eliminate  $l$  from the equation for the maximum flux  $\Phi_{\max}$ . Equation (10) may be rewritten by going to the limits  $\Phi_{\max 2}$  for  $\Phi_{\max}$  and  $l_2$  for  $l$

$$\Phi_{\max 2} = \frac{B_{\max 1}}{\sqrt{2} c} \left[ 1 + \sqrt{2} c l_2 \cos (45^\circ + \alpha_2) \right] \quad (10a)$$

or, when equation (15a) is used,

$$\Phi_{\max 2} = \frac{B_{\max 1}}{\sqrt{2} c} \sqrt{1 + 2 \cos (45^\circ + \alpha_2) \left( \frac{H_{\max 2}}{H_{\max 1}} - 1 \right)} \quad (10b)$$

The argument involved for obtaining the current  $I_{\max 2}$  is identical to that used for equation (9); the replacement therefore of  $H_{\max s}$  by  $H_{\max 2}$  in equation (9) gives the expression for  $I_{\max 2}$

$$H_{\max 2} = 0.4 \pi I_{\max 2} \quad (17)$$

where

$I_{\max 2}$  value in SYMBOLS (also, current in amperes required in one-turn energizing coil to furnish given impressed field intensity  $H_{\max 2}$  for volume of plate having surface 1 cm square and depth equal to one-half plate thickness), amperes per centimeter

The effective value of current  $I_2$  for an assumed sine wave is

$$I_2 = \frac{I_{\max 2}}{\sqrt{2}} = \frac{H_{\max 2}}{\sqrt{2} 0.4\pi} \quad (17a)$$

The remaining derivation is that of the power-factor angle, which will be obtained by finding first the angle  $\delta_2$  and then  $\beta_2$ . The derivation of  $\delta_2$  and  $\beta_2$  may be found in appendix A.

$$\delta_2 = \frac{\tan(45^\circ + \alpha_2)}{2} \log_e \left[ 1 + 2 \cos(45^\circ + \alpha_2) \left( \frac{H_{\max 2}}{H_{\max 1}} - 1 \right) \right] \quad (18)$$

and

$$\beta_2 = \cot(45^\circ + \alpha_2) \log_e \left[ 1 + \sin(45^\circ + \alpha_2) \left( \frac{H_{\max 2}}{H_{\max 1}} - 1 \right) \right] \quad (19)$$

For a given value of  $H_{\max 2}/H_{\max 1}$ , various values of  $\alpha_2$  were substituted in equations (18) and (19) until, by successive approximations, an average value of  $\alpha_2$  was obtained that satisfied the equation

$$\alpha_2 = \frac{\int_0^{(\beta_2)_a} (\beta_2 - \delta_2) d(\beta_2)}{(\beta_2)_a}$$

where  $(\beta_2)_a$  is the limit of integration. The resulting values of  $\beta_2 - \delta_2$  are shown as a function of  $\beta_2$  in figure 7. The values of  $H_{\max 2}/H_{\max 1}$  and  $\alpha_2$  are posted beside each calculated point. Replots of the data from figure 7 are presented in figures 8 and 9. In figure 8 the angle  $\alpha_2$  is presented as a function of various values of  $H_{\max 2}/H_{\max 1}$ , and figure 9 shows the angle  $\beta_2 - \delta_2$  as a function of  $H_{\max 2}/H_{\max 1}$ .

# Results of Analysis

The eddy-current power  $p_e$  absorbed as heat per square centimeter of plate surface will be the product of the voltage, the current, and the power factor (fig. 6) and may be expressed as

$$p_e = E_2 I_2 \sin (45^\circ + \beta_2 - \delta_2)$$

or from equations (16a) and (17a)

$$p_e = f(10^{-8}) \frac{B_{\max 1}}{c} \sqrt{1 + 2 \cos (45^\circ + \alpha_2) \left( \frac{H_{\max 2}}{H_{\max 1}} - 1 \right)} \frac{H_{\max 2}}{\sqrt{2} 0.4} \sin (45^\circ + \beta_2 - \delta_2)$$

Revision yields

$$p_e = \frac{1.25 \sqrt{2} f H_{\max 2} B_{\max 1} 10^{-8}}{c} \sqrt{1 + 2 \cos (45^\circ + \alpha_2) \left( \frac{H_{\max 2}}{H_{\max 1}} - 1 \right)} \sin (45^\circ + \beta_2 - \delta_2) \quad (20)$$

Replacement of  $c$  by its parts yields

$$p_e = \frac{1.25 \sqrt{5}}{\pi} \frac{1}{\rho} \frac{1}{f} \frac{1}{2} H_{\max 2} B_{\max 1} 10^{-4} \sqrt{\frac{1}{\mu} [1 - 2 \cos (45^\circ + \alpha_2)] + 2 \cos (45^\circ + \alpha_2) \frac{H_{\max 2}}{B_{\max 1}}} \sin (45^\circ + \beta_2 - \delta_2) \quad (20a)$$

watts per square centimeter

where  $\rho$  is resistivity (ohm-cm). Multiplying equation (20) by 6.45 gives the equation for the heat generated per square inch.

$$p_e' = \frac{11.4 f H_{\max 2} B_{\max 1} 10^{-8}}{c} \sqrt{1 + 2 \cos (45^\circ + \alpha_2) \left( \frac{H_{\max 2}}{H_{\max 1}} - 1 \right)} \sin (45^\circ + \beta_2 - \delta_2), \text{ watts per square inch} \quad (20b)$$



### Operation at Constant Permeability

The equations that have been derived are not limited in use to conditions in which the outer plate surface is saturated, but are also applicable in the region of the approximated magnetization curve where the permeability  $\mu$  is constant. At the saturation point, where  $H_{\max 2}$  is equal to  $H_{\max 1}$ , the equation for the total depth of penetration (equation (15c)) reduces to equation (7a). The depth of penetration remains constant at the value given by equation (7a), even if the impressed field is reduced below  $H_{\max 1}$ . The power-factor angle  $\theta$  remains  $45^\circ$  for field intensities equal to or less than  $H_{\max 1}$ , and  $\beta_2$  and  $\delta_2$  vanish. At the saturation point, the radical in the voltage equation (16a), the total-flux equation (10b), and the power equation (20b) reduces to a value of 1. These equations are still applicable for impressed field intensities less than  $H_{\max 1}$  with the substitution of the impressed field intensity  $H_{\max s}$  for  $H_{\max 2}$  and the value equivalent to the impressed field  $B_{\max s}$  for  $B_{\max 1}$  after the radical has been replaced by 1. The total-flux equation (10b) reduces to equation (4a). The current formula (17a) applies if the given impressed field intensity  $H_{\max s}$  is used for  $H_{\max 2}$ .

### EXPERIMENTAL INVESTIGATION

Prior to any attempt at full-scale application of eddy-current heating of the inlet guide vanes, preliminary investigations were conducted from which information was obtained as to the number of field ampere turns required to produce specified amounts of heat.

The schematic layout of the equipment in which sample blades were investigated is shown in figure 10. For simplicity, instead of using a chopper to vary the flux, a similar effect was accomplished by varying the magnetomotive force or ampere turns by connecting the coil shown in figure 10 to a 500-watt, 6100-cycle-per-second, audio-frequency power generator. In order to match the load to the generator properly, the turns on the coil were varied from 316 to 210, in addition to resonating this load with series capacitors. The current in the coil was measured with radio-frequency ammeters.

The heat generated was determined by measuring the temperature rise and the rate of water flowing through the jacket. Heat exchange to the laminated core was minimized by keeping the core

temperature near the mean temperature of the water. From runs with and without insulation, insulation on the water jacket to reduce heat transfer between the atmosphere and the jacket apparently was unnecessary in this investigation.

The pulsating unidirectional operation was synthesized by superimposing a direct current and an alternating current in the inductor of the experimental unit, as shown in figure 11. The direct current to the inductor was introduced by means of a filtering network. The 0.55-henry choke, which was especially wound with a large air gap to prevent saturation, had approximately 10 times the inductance of the inductor and thus shunted only about 10 percent of the alternating current from the inductor. The inductance value of the remaining choke was not critical, but its impedance was sufficient, relative to the 20-microfarad condenser, to force most of the alternating current of the 0.55-henry choke through the measuring meter in series with the 20-microfarad condenser. Because the ratio of inductive reactance to resistance of the 0.55-henry choke and the inductor are sufficiently alike to make the currents in phase for all practical purposes, the difference between the readings of the two alternating-current ammeters was therefore the alternating current in the inductor. No appreciable alternating current passed through the direct-current ammeter or the battery circuit and the direct-current meter read the true direct current applied to the inductor.

The first investigations were made on annealed SAE 1020 steel with a total air gap between the laminated iron core and a sample blade of approximately 0.04 inch. The air gaps used for these investigations were approximately those that would exist in practice between the blade and the adjacent part through which the flux would flow. In order to permit a correlation between experimental results and the analysis, the blades were made of rectangular cross section. The actual size of the sample, however, which was 0.125 by 1 by  $4\frac{5}{8}$  inches, is approximately the same as the inlet guide vanes of a typical axial-flow compressor. The second and third experiments were made with a blade of Armco Magnetic Ingot Iron of the same size. In the second experiment, the air gap was kept at approximately 0.04 inch and in the third experiment the air gap was increased to approximately 0.06 inch. A sample of Hipernik, 0.094 by 1 by  $4\frac{5}{8}$  inches, with a total air gap of 0.04 inch was used in the fourth experiment. This material has high resistivity and high maximum flux density. The investigations on all samples were made by varying the number of magnetizing ampere turns and measuring the heat generated.

The fifth experiment was made with the synthesized pulsating unidirectional current. As illustrated by the curve in figure 11, the two currents were apportioned to subject the blade to a magnetomotive force that varied from 0 to  $2\sqrt{2}$  times the root-mean-square value of alternating magnetomotive force at each experimental condition. The Armco iron sample was used in this investigation and the total air-gap spacing was 0.04 inch.

A 10-turn search coil was placed around the center of the sample blade in all experiments for the purpose of measuring the voltage and viewing the voltage wave shape on a cathode-ray oscilloscope. Ten turns were used to obtain sufficient signal voltage to make the hum voltage and other spurious voltages negligible in comparison.

#### CALCULATION OF AMPERE TURNS

The correlation between the analytical equations and the experimental results depends on several new calculations that must be made in addition to computations using the equations already derived.

The blade was positioned in the experimental rig (fig. 10) to make the air gaps at each end of the blade approximately equal. Figure 12 shows the geometry used in calculating the permeances at each blade end. No attempt was made to draw figure 12 to scale or to make the relative sizes of the various volumes correct. (Volumes are designated by numbers 1 to 8.) The purpose of the figure is to give the geometric shapes of the various volumes to illustrate the application of formulas from reference 6. The suggestion given in this reference was followed in limiting the fringing-flux calculations to the entire space immediately surrounding the pole faces and not at a great distance along the blade ( $h+t+g$  was limited to approximately 0.75 in., where  $h$ ,  $t$ , and  $g$  are dimensions, as shown in fig. 12). The geometry of figure 12 is based on the two propositions that the flux lines are normal to the metal surfaces and that such surfaces are equipotential. These propositions are obviously assumptions, because the magnetomotive-force drop along 0.75 inch of blade is appreciable.

The formulas for the permeances of the various volumes designated by the numbers in figure 12 follow for convenience. The air gap directly under the blade was assumed to have no flux, except for a volume equivalent to the depth of penetration. This permeance  $P_1$  was therefore taken to be equal to the product of the depth of penetration  $l_T$  and the circumference of the blade cross section, divided by the distance  $g$ :

$$P_1 = \frac{2l_T(d+w)}{g}$$

where  $w$  refers to width, as shown in figure 12. Also

$$P_2 = 0.52 w$$

$$P_3 = \frac{2w}{\pi} \log_e \left( \frac{g+t}{g} \right)$$

The plane ABC is so positioned that the average value of volume 5 remains unchanged. In this manner, volumes 4 and 5 can be combined in one calculation. On a scale drawing, the line BA was found to make an angle of  $50^\circ$  with the horizontal, the angle ABD therefore being  $140^\circ$ . Then

$$P_{4+5} = \left( \frac{180}{140} \right) \frac{w}{\pi} \log_e \left( \frac{g+h+t}{g+t} \right) = \frac{1.28 w}{\pi} \log_e \left( \frac{g+h+t}{g+t} \right)$$

and

$$P_6 = 0.52 d$$

$$P_7 = \frac{2d}{\pi} \log_e \left( \frac{g+t+h}{g} \right)$$

Volume 8 is considered a partial quadrant of a spherical shell of thickness  $t+h$ . The fraction used as a factor in making the computation is the ratio between 180 and the arithmetic mean of 140 and 90, or

$$P_8 = \frac{180}{\left( \frac{140+90}{2} \right)} \frac{t+h}{4} = 0.39(t+h)$$

The total permeance for one end will be

$$2 \left( \frac{P_1}{2} + P_2 + P_3 + P_{4+5} + P_6 + P_7 + 2P_8 \right)$$

The total air-gap permeance will equal one-half of this value, or

$$P_T = \frac{P_1}{2} + P_2 + P_3 + P_4 + P_5 + P_6 + P_7 + 2P_8 \quad (21)$$

The following equation can be written from the total-air-gap magnetomotive-force equation for the real component

$$N_a I_{\max a} = \frac{A}{0.4 \pi l_o} \frac{\Phi_{\max 2} \cos(45^\circ + \beta_2 - \delta_2)}{P_T}$$

Substitution of equation (10b) gives the equation for air-gap ampere turns

$$N_a I_{\max a} = \frac{A}{0.4 \pi \sqrt{2} c l_o} \frac{\cos(45^\circ + \beta_2 - \delta_2) B_{\max 1}}{P_T} \sqrt{1 + 2 \cos(45^\circ + \alpha_2) \left( \frac{H_{\max 2}}{H_{\max 1}} - 1 \right)} \quad (22)$$

The final determination needed is that for the magnetomotive-force drop along the blade. Previous discussion showed that the flux density at the outer surface of the blade is the result of the impressed magnetomotive force alone; the following equation is therefore true:

$$H_{\max 2} = \frac{0.4 \pi N_b I_{\max b}}{L}$$

Thus

$$N_b I_{\max b} = \frac{L H_{\max 2}}{0.4 \pi} \quad (23)$$

The total effective ampere turns required are

$$NI = \frac{N_a I_{\max a} + N_b I_{\max b}}{\sqrt{2}} \quad (24)$$

When the previously derived equations are used, the eddy-current power per square inch of blade surface appearing as heat can be calculated from equation (20b), and the voltage can be

determined from equation (16a). The total depth of penetration of the flux into the blade is found from equation (15c).

Values of  $H_{\max 2}$  selected for making check calculations were 6, 30, and 50 oersteds. These values are shown in figure 4 for SAE 1020 steel, together with the corresponding values of 11,500, 15,000, and 15,800 gaussses for the average values of  $B_{\max 1}$ . The permeability of the left part of the magnetization curve, which is the slope of the line AF, is 2665. The magnetization curve for Armco Magnetic Ingot Iron (reference 7) and lines BC, DE, and FG indicating the average values of  $B_{\max 1}$  chosen for 6, 30, and 50 oersteds, respectively, are shown in figure 13.

The magnetization curve for Hipernik (from reference 8), which has relatively high resistivity, is shown in figure 14. The horizontal lines BC, DE, and FG on this curve represent chosen average values of  $B_{\max 1}$  of 12,800, 14,000, and 15,000 gaussses for limiting field intensities  $H_{\max 2}$  of 6, 20, and 40 oersteds, respectively.

## RESULTS AND DISCUSSION

### Electrical Considerations

Results of the calculations and the experiments are given in table I and plotted in figures 15 and 16. Figure 15 is a plot of voltage at the surface per centimeter width of blade against effective impressed ampere turns. The search coil around the center of the blade is the source of the voltage data, which are divided by the product of coil turns and blade cross-sectional circumference in centimeters to obtain the values for the plotted points. The curves are for investigations on SAE 1020 steel, Armco Iron, and Hipernik, each with total air gaps of 0.04 inch. Calculated values of voltages from equation (16a) for field intensities at the blade surface of 6, 30, and 50 oersteds are also plotted on figure 15 for Armco Iron and SAE 1020 steel. The limiting field intensities used in making voltage calculations for Hipernik were 6, 20, and 40 oersteds. The root-mean-square or effective ampere turns for each intensity were calculated from equations (24), (23), and (22). The purpose of these data is to show the close agreement between calculated and measured voltages. The numerical comparison between calculated and measured voltages obtained from columns 10 and 11, respectively, of table I shows agreement to within 10 percent, except for Hipernik where the disagreement is approximately 16 percent. The magnetization data used in the calculations, however, came from published

average curves that may not exactly represent the samples inasmuch as the measured conductivity of the samples used in the calculations did not agree with the published average data.

Three of the curves in figure 16, which represents eddy-current power generated per square inch of blade surface plotted against effective impressed ampere turns, are for SAE 1020 steel, Armco Magnetic Ingot Iron, and Hipernik for a total air gap of 0.04 inch. Figure 16 shows the close correlation between the curves and plotted check points obtained from analytical formula (20b) for field intensities at the blade surface of 6, 30, and 50 oersteds for Armco Iron and SAE 1020 steel and 6, 20, and 40 oersteds for Hipernik. Again the root-mean-square ampere turns for each of these intensities were calculated from equations (24), (23), and (22). From columns 12 and 13 of table I, the agreement between calculated and measured values is within 10 percent.

On the Armco Iron curve for a total air gap of 0.04 inch (fig. 16), the data of the synthesized-pulsating-flux investigations are plotted. The measured eddy-current power is plotted against the root-mean-square value of the alternating component of current. These points agree closely with the simple alternating-current tests and indicate that the superposition of the direct-current magnetomotive-force component has very little effect if any. It is important to understand, however, as the curve in figure 11 demonstrates, that for any given power the ampere turns from figure 16 must be increased by a factor of  $2\sqrt{2}$  to obtain the direct-current ampere turns needed for use with a chopper.

The ineffectiveness of the direct current to change conditions is further demonstrated by comparison of the voltage-wave shapes obtained with and without the superimposed direct current. These curves, which are shown in figure 17, are oscillograms from the search coil around the center of the blade. One set of records is for low values of ampere turns and the other set is for high values.

A voltage survey along the blade (fig. 10) with this search coil indicated voltage variations of 14 percent at the bottom to -25 percent at the top compared with the value at the blade center. The value at the blade center used for data, was, however, approximately equal to the average value along the blade. The inequality of the flux along the blade is believed to be due to the fringing flux from the off-center exciting coil (fig. 10).

The large magnetomotive-force drop across the blade probably explains the ability of the coil fringing flux to affect the voltage along the blade. The magnetomotive-force data are obtained

from columns 7, 8, and 9 of table I, in which the air-gap maximum ampere turns, the blade maximum ampere turns, and the total root-mean-square ampere turns, respectively, are given. These data show that as the blade-surface field intensities increase the air-gap ampere turns  $N_a I_{\max a}$  decrease from approximately 30 percent to about 10 percent of the blade ampere turns  $N_b I_{\max b}$ . Below 6 oersteds, of course, the percentage of air-gap ampere turns is still larger. The large drop across the blade comes from operation well past the knee of the magnetization curve at the blade surface. Inspection of figures 4, 13, and 14 shows the knee of the magnetization curves to be in the neighborhood of 6 oersteds or lower, which is equivalent to the very low value of approximately 50 ampere turns on the curves of figure 16. It is recognized that this large magnetomotive-force drop along the blade in comparison with air gaps of practical sizes may make a difficult chopper-design problem; that is, it may be difficult to obtain sufficient chopping action at relatively high frequencies.

Two curves for Armco Iron are shown in figure 16, the one previously discussed for a total air gap of 0.04 inch and the other for an air gap of 0.06 inch. These two curves show that the fringing flux around the air gap is very important and, because of the fringing, the air-gap spacing between a tooth and a blade is not a critical factor in determining the maximum flux or the total heat generated in the blade. For this reason, relatively large clearances between blade and tooth can be accommodated if dictated by compressor-design criterions; however, fringing flux may also contribute to chopper-design difficulties by limiting reluctance change in the air gap.

Calculated data also indicate that the flux that fringes around the air gap is the major portion of the flux. The calculated permeance (table I, column 5) including the fringing space is approximately 9.00 centimeters; whereas the approximate permeance of the air gap alone, depending upon the depth of penetration, is only 0.5 to 1.0 centimeter. The depth of penetration is given in column 6 of table I and varies from about 0.005 centimeter at a blade-surface field intensity  $H_{\max 2}$  of 6 oersteds to about 0.015 centimeter at 50 oersteds for Armco Iron and SAE 1020 steel. A direct result of the lower conductivity of Hipernik is that its depth of penetration is equal to twice that of the other materials.

Equation (20a) will now be examined for the purpose of discussing the various parameters involved. At the field intensities



of interest, those that will produce 10 or 11 watts per square inch, the first quantity under the radical of the equation is less than 5 percent of the radical value and can therefore be neglected. The equation reduces to

$$p_e = \left[ \frac{1.25\sqrt{5}}{\pi} \sin(45^\circ + \beta_2 - \delta_2) 10^{-4} \sqrt{2 \cos(45^\circ + \alpha_2)} \right] \rho^{\frac{1}{2}} f^{\frac{1}{2}} (H_{\max 2})^{\frac{3}{2}} (B_{\max 1})^{\frac{1}{2}} \quad (20c)$$

Also, at the field intensities of interest the values of  $\alpha_2$  and  $\beta_2 - \delta_2$  change very little, which can be seen from columns 3 and 4 of table I for values of  $H_{\max 2}$  of 30 and 50. A noteworthy fact is that the angle  $(45^\circ + \beta_2 - \delta_2)$ , the sine of which is the power factor, changes only from  $45^\circ$  to about  $55^\circ$  over the entire range of field intensity  $H_{\max 2}$  of 0 to 50. The sine  $(45^\circ + \beta_2 - \delta_2)$  and  $\sqrt{2 \cos(45^\circ + \alpha_2)}$  are therefore grouped in the brackets of equation (20c) with the other constants. Equation (20c) therefore gives very simply the factors that determine the ability of a material to produce heat from eddy currents. For a given value of field intensity  $H_{\max 2}$  or magnetizing ampere turns, the eddy current generated per unit surface is proportional to the square roots of the resistivity of the material, the saturation flux density, and the frequency. For a given material and frequency, the heat generated is proportional to the  $3/2$  power of the magnetizing ampere turns. Provided the blade is sufficiently thick to make the flux at the center negligible, equation (20c) shows that the heating is independent of blade thickness and is a function of surface area only. Because cooling is also a function of surface area, however, the important criterion is the heat generated per unit surface rather than the total heat, and in this report equations and results are therefore expressed in values per unit surface.

Because for a given installation the highest usable frequency is fixed by the geometry of the compressor, for a required amount of heat the variables will be the saturation flux density  $B_{\max 1}$ , the ampere turns  $NI$ , and the resistivity of the material  $\rho$ , or

$$H_{\max 2} = F(NI) = \frac{\text{constant}}{\sqrt[3]{\rho B_{\max 1}}}$$

This equation shows that a blade material having high resistivity and high saturation flux density is desirable in the interest of keeping the impressed ampere turns at a minimum, because the number of ampere turns required varies inversely as the cube roots of the resistivity and the saturation flux density.

The advantage of a high-resistivity material is experimentally shown by the curve for Hipernik in figure 16. The resistivity of Hipernik, which is about four times the resistivity of Armco Iron, is the determining factor in reducing the required impressed ampere turns for Hipernik relative to Armco Iron for a given heat density. As previously indicated, Hipernik has higher flux penetration because of its greater resistivity relative to the other two materials; the greater depth of eddy currents is the mechanism explaining the larger heat density. The use of a higher-resistivity material should help the solution of the chopper problem previously mentioned.

From the data of figure 16 and for other assumed conditions, the direct-current power required for producing the magnetizing current can be roughly estimated. For one such theoretical installation, the magnetizing power required per square inch of blade surface to produce a heat value of 10 watts per square inch was 0.1 watt, or approximately 1 percent. Calculations were then made to determine whether the power required for ice protection would exceed that available from such a system of eddy-current heating.

#### Calculation of Heat Required

Inasmuch as the proposed system of eddy-current heating of the axial-flow compressor-inlet guide vanes is dependent upon a revolving rotor, rotor speeds had to be specified for the computation of the heat required. No icing tolerances were allowed. Because the severity of icing may prove to be a function of altitude and air consumption, the heat requirements for several engine conditions and altitudes were also studied.

The rate of heat dissipation was computed for the conditions subsequently enumerated. The analysis employed was taken from references 9 to 11 and is presented in appendix B for convenience. The blade-surface temperature was assumed to be kept at 35° F and the temperature of the compressor-inlet air was assumed to be 0° F. The aircraft was assumed to be flying at a true airspeed of 275 miles

per hour through air having a liquid-water content of 1 gram per cubic meter. Heat requirements were then calculated for an axial-flow compressor of the 4000-pound-thrust class for the following conditions:

Altitude (ft)	Engine speed (rpm)	Air flow (lb/sec)
0	7600	75
	7000	65
	6000	50
5,000	7600	65
	7000	50
	6000	45
15,000	7600	50
	7000	45
	6000	35

The rate of heat dissipation was the greatest for the highest speed condition at sea level (fig. 18(a)). The average heat dissipation for this condition was approximately 5400 Btu per hour per square foot, which is equivalent to a power of approximately 11 watts per square inch of vane surface.

#### Shaft Power Required

The power required for protecting the inlet guide vanes under the design conditions is approximately 11.6 horsepower or about 8.7 kilowatts. At sea level and at rated engine speed of 7600 rpm, the compressor absorbs about 5680 horsepower. Thus the power required for protection against ice accretion would be only about 0.20 percent of the turbine load. In addition to the power furnished by the turbine, about 1 percent of the 11.6 horsepower required for protection will necessarily be supplied for excitation of the coils. The electric power for excitation can be supplied by batteries and generator.

#### Apparent Advantages and Disadvantages

The apparent advantages of an ice-protection system utilizing eddy-current heating lie in the fact that heat is produced where

needed with little time lag. Most of the heat is used to warm the surface subject to icing and not the induction air as in the exhaust bleedback systems. The loss in net thrust would therefore be small because the increase in the temperature of the incoming mass of induction air due to surface heating would be slight.

If ice accumulations occur before heat is applied, de-icing can be accomplished because eddy-current heating will melt the under surface of the ice coating and permit washing-back of the accumulated ice by the induction air. This washing-back may prove to be a disadvantage, however, if the pieces broken off are allowed to become large enough to damage the compressor blading. The application of some heat before the ice is allowed to accumulate may therefore be necessary.

Because no special ducting is required for eddy-current heating, the design may be kept within the limits of the maximum diameter of the compressor. Eddy-current heating may have to be supplemented with some other system of heating, however, to protect the lips and the surface of the inlet cowling. Corrosive exhaust gases need not be fed back into the compressor, however, because they can be contained within the walls of the inlet.

The modifications with eddy-current heating appear feasible. The system of protection by means of eddy-current heating can be applied back through the compressor for as many stages as is deemed necessary. The heat requirement for successive stages would diminish with stage number. Application of this principle, however, becomes more difficult with successive stages because of limited clearances and complexity of electric circuits.

With eddy-current heating, the use of intensity-controlled heating would be possible because the controls would be simple.

The disadvantages of the application of eddy-current heating are the necessity for including magnetic material in the flux circuit and the corresponding weight increase of these materials and of the coil and the chopper.

#### SUMMARY OF RESULTS

From an investigation of eddy-current heating for icing protection of axial-flow-compressor blades, the following results were obtained:

1. Heating of axial-flow-compressor blades by eddy currents appeared to be applicable for protection against icing.

2. The surface average heat requirement for the inlet guide vanes in conditions of icing of a jet engine of the 4000-pound-thrust class was calculated to be maximum at rated-speed conditions and equal to 5400 Btu per hour per square foot or approximately 11 watts per square inch. Creation of heat densities of this magnitude for ice protection of the inlet-guide vanes of a compressor appeared possible.

3. The shaft-power requirement for the generation of eddy currents to produce the heat needed for protection of the inlet guide vanes is small, and for the proposed design is only 0.20 percent of the turbine load. Compared to this power, the electrical power required for the magnetizing field coils, however, is only of the order of 1 percent of the shaft power required for generation of the eddy currents or 0.002 percent of the turbine load.

4. In an alternating-flux eddy-current system at heat densities necessary for ice protection, the eddy-current power generated is proportional to the square roots of frequency, material resistivity, and saturation flux density, and to the  $3/2$  power of the maximum field intensity at the vane surface. The blade material chosen should therefore have the highest resistivity and the greatest saturation flux density.

5. In a pulsating-unidirectional flux eddy-current system in which the flux varies from zero to a maximum value and which can be simulated by superimposing a direct-current flux on a sine-wave alternating-current flux, the heat generated does not change appreciably with application of the direct-current flux. Heat calculations can therefore be made on the basis of the alternating-current component. In the production of the pulsating flux by means of a chopper and the application of a direct-current magnetomotive force, however, the required direct-current ampere turns will be greater than the root-mean-square ampere turns of the alternating-current component by a factor of  $2\sqrt{2}$ .

6. The vane surfaces will probably operate well past the knee of the magnetization curve of the blade material, and the magnetomotive-force drop along the blade will be great in comparison with air gaps of practical sizes, which may lead to difficulty in obtaining sufficient chopping action at high frequencies.

7. Provided that the blade is sufficiently thick to insure a negligible flux at the center, the heat generated per unit surface is independent of vane thickness or the total heat generated is a function of only the vane surface.

8. The disadvantages anticipated in the application of eddy-current heating would be the necessity for including magnetic material in the flux circuit and the corresponding weight increase of these materials and of the coil and the chopper.

Lewis Flight Propulsion Laboratory,  
National Advisory Committee for Aeronautics,  
Cleveland, Ohio.

## APPENDIX A

DERIVATION OF ANGLES  $\delta_2$  AND  $\beta_2$ 

From figure 6,

$$\Phi_{\max} d\delta = E_{\max} l \, dl \sin (45^\circ + \beta - \delta) \quad (A1)$$

or, using equation (10),

$$\begin{aligned} d\delta &= \frac{E_{\max} l \, dl \sin (45^\circ + \beta - \delta)}{\frac{E_{\max} l}{\sqrt{2} c} + \int E_{\max} l \, dl \cos (45^\circ + \beta - \delta)} \\ &= \frac{\sin (45^\circ + \beta - \delta)}{\cos (45^\circ + \beta - \delta)} \frac{\sqrt{2} c \, dl \cos (45^\circ + \beta - \delta)}{1 + \int \sqrt{2} c \, dl \cos (45^\circ + \beta - \delta)} \quad (A2) \end{aligned}$$

Integrating in the limits 0 to  $\delta_2$  and 0 to  $l_2$ ,

$$\delta_2 = \tan (45^\circ + \alpha_2) \log_e \left[ 1 + \sqrt{2} c \cos (45^\circ + \alpha_2) l_2 \right] \quad (A3)$$

where  $\alpha_2$  is the mean value of  $\beta_2 - \delta_2$  for the given value of  $l_2$ , which gives from equation (15a)

$$\delta_2 = \frac{\tan (45^\circ + \alpha_2)}{2} \log_e \left[ 1 + 2 \cos (45^\circ + \alpha_2) \left( \frac{H_{\max 2}}{H_{\max 1}} - 1 \right) \right] \quad (A4)$$

The derivation of  $\beta_2$  follows a similar procedure. In figure 6, the increment of current in each new sheet of material of thickness  $dl$  is equal to the product of induced voltage and the conductance of the sheet, or  $\gamma E_{\max} dl$ ; therefore,

$$\begin{aligned} I_{\max} &= I_{\max 1} + \int \gamma E_{\max} dl \sin (45^\circ + \beta - \delta) \\ &= \frac{E_{\max} l}{0.4\pi} + \int \gamma E_{\max} dl \sin (45^\circ + \beta - \delta) \quad (A5) \end{aligned}$$

From the vector diagram, the following relation is true:

$$I_{\max} d\beta = \gamma E_{\max} dl \cos (45^\circ + \beta - \delta) \quad (A6)$$

or, when equations (A5) and (A6) are combined,

$$d\beta = \frac{\cos (45^\circ + \beta - \delta)}{\sin (45^\circ + \beta - \delta)} \frac{\frac{0.4 \pi \gamma E_{\max}}{H_{\max} l} dl \sin (45^\circ + \beta - \delta)}{1 + \int \frac{0.4 \pi \gamma E_{\max}}{H_{\max} l} dl \sin (45^\circ + \beta - \delta)} \quad (A7)$$

Integrating from 0 to  $\beta_2$  and from 0 to  $l_2$ , where  $\alpha_2$  is the average of  $\beta_2 - \delta_2$  as before, yields

$$\beta_2 = \cot (45^\circ + \alpha_2) \log_e \left[ 1 + \int_0^{l_2} \frac{0.4 \pi \gamma E_{\max}}{H_{\max} l} dl \sin (45^\circ + \beta - \delta) \right] \quad (A8)$$

The first step in the evaluation of the integral is to replace  $E_{\max}$  by using equations (10) and (12).

$$\int_0^{l_2} \frac{0.4 \pi \gamma E_{\max}}{H_{\max} l} dl \sin (45^\circ + \beta - \delta) =$$

$$\int_0^{l_2} \frac{0.4 \pi \gamma 2\pi f 10^{-8}}{H_{\max} l} \left[ \frac{B_{\max} l}{\sqrt{2} c} + B_{\max} l \cos (45^\circ + \alpha) \right] dl \sin (45^\circ + \beta - \delta)$$

or

$$= \int_0^{l_2} \left[ \sqrt{2} c + 2c^2 l \cos (45^\circ + \alpha) \right] dl \sin (45^\circ + \beta - \delta)$$

or where  $\alpha$  is again the average value of  $(\beta - \delta)$ ,

(A9)

$$\int_0^{l_2} \frac{0.4 \pi \gamma E_{\max}}{H_{\max} l} dl \sin (45^\circ + \beta - \delta) = \left[ \sqrt{2} c l_2 + c^2 l_2^2 \cos (45^\circ + \alpha_2) \right] \sin (45^\circ + \alpha_2)$$



With substitution of equation (A9), equation (A8) becomes

$$\beta_2 = \cot(45^\circ + \alpha_2) \log_e \left\{ 1 + \left[ \sqrt{2} c l_2 + c^2 l_2^2 \cos(45^\circ + \alpha_2) \right] \sin(45^\circ + \alpha_2) \right\} \quad (A10)$$

Substitution of equation (15b) into equation (A10) gives the solution for  $\beta_2$

$$\beta_2 = \cot(45^\circ + \alpha_2) \log_e \left[ 1 + \sin(45^\circ + \alpha_2) \left( \frac{H_{\max 2}}{H_{\max 1}} - 1 \right) \right] \quad (A11)$$

## APPENDIX B

CALCULATION OF RATE OF HEAT REQUIRED TO MAINTAIN SPECIFIED  
BLADE-SURFACE TEMPERATURE IN CONDITIONS OF ICING

An analysis of the heating requirements for thermal-ice prevention of the inlet guide vane of an axial-flow compressor is presented for specified conditions of icing. The feasibility of a design of an ice-prevention system utilizing eddy-current heating under the assumed icing conditions has been presented in the text of this report.

## Symbols

The following symbols are used in this appendix:

A	cross-sectional area of flow passage, sq ft
C	blade chord, ft
$c_p$	specific heat of air at constant pressure, Btu/(lb)(°F)
$c_{p,w}$	specific heat of water, Btu/(lb)(°F)
D	diameter of equivalent leading-edge cylinder, ft
d	average distance between adjacent blades, ft
e	vapor pressure, lb/sq in.
$e_s$	vapor pressure at saturation at temperature of surface, lb/sq in.
$e_x$	local vapor pressure, determined by equation (B9), lb/sq in.
g	acceleration due to gravity, 32.2 ft/sec <sup>2</sup>
H	total heat dissipation, Btu/(hr)(sq ft)
$H_1$	heat dissipation due to convection, Btu/(hr)(sq ft)
$H_2$	heat dissipation due to evaporation, Btu/(hr)(sq ft)
$H_3$	heat dissipation due to heating of impinging water on surface of blade, Btu/(hr)(sq ft)

$h$	unit thermal convective conductance between vane surface and air, $\text{Btu}/(\text{hr})(\text{sq ft})(^{\circ}\text{F})$
$J$	mechanical equivalent of heat, $\text{ft-lb}/\text{Btu}$
$L$	latent heat of vaporization of water, $\text{Btu}/\text{lb}$
$l$	length of blade, $\text{ft}$
$M$	water impingement per unit area, $\text{lb}/(\text{hr})(\text{sq ft})$
$M_e$	water impingement per unit area leading edge, $\text{lb}/(\text{hr})(\text{sq ft})$
$M_s$	water impingement per unit area blade surface, $\text{lb}/(\text{hr})(\text{sq ft})$
$m$	liquid-water content, $\text{lb}/\text{cu ft}$
$N$	number of blades
$Pr$	Prandtl number
$p$	static pressure, $\text{lb}/\text{sq in. absolute}$
$R$	gas constant, for air $53.3 \text{ ft-lb}/(\text{lb})(^{\circ}\text{R})$
$s$	distance along chord from leading edge of blade, $\text{ft}$
$T_{av}$	average of inlet-air temperature and blade-surface temperature, $^{\circ}\text{R}$
$t$	air temperature, $^{\circ}\text{F}$
$t_s$	surface temperature with no external heat conditions, $^{\circ}\text{F}$
$t_{s d}$	surface design temperature, $^{\circ}\text{F}$
$V$	velocity, $\text{ft}/\text{sec}$
$W$	air flow, $\text{lb}/\text{sec}$
$x$	average distance between adjacent blades, $\text{ft}$
$\alpha$	angle of attack of blade section, degrees
$\gamma$	ratio of specific heats, for air = 1.4
$\rho$	density, $\text{slugs}/\text{cu ft}$

## Subscripts:

- c     compressor inlet
- s     surface condition
- x     local condition at any chordwise position on blade surface

## Liquid Water in Atmosphere

The basis for the design of an ice-prevention system was established from recent and extensive information on the severity of icing conditions likely to be experienced by an airplane under normal engine operation (reference 9). The icing condition selected may occur in cumulus clouds having a liquid-water content of 1.0 gram per cubic meter and an average drop size of 20 microns in diameter. The inlet temperature was assumed to be 0° F.

## Impingement of Water on an Airfoil

Little information is available regarding the impingement of water on airfoils as small as those found at the inlet of an axial-flow compressor of the type studied herein. Limited use was therefore made of the existing theory involving much larger airfoils, such as propeller blades and wings. Figure 19 indicates the shape and dimensions of the inlet-guide vanes considered in this report. Eighty-eight such blades are at the compressor inlet. The water impingement was assumed to be confined to the leading edge and the concave surface of the vane and, because the vanes are small, their collection efficiency was further assumed to be 100 percent.

The specific conditions for which the rate of heat required is calculated are for a compressor-inlet air temperature of 0° F and a vane-design surface temperature of 35° F. The temperature and the pressure of the air passing over the first row of vanes differ from the inlet-air temperature and pressure because of kinetic effects and are functions of air velocity and density.

Velocity gradient through blading. - Any two adjacent blades of the same compressor stage, because of their shape and spacing, can be assumed to constitute a nozzle. The cross-sectional areas used for computation of the average air velocity over each section of blade can be determined using average values of the distance between adjacent blade surfaces.

The section flow area is

$$A_x = l d_x \quad (B1)$$

The spanwise average air velocity through a passage at any blade section is then

$$V_x = \frac{W}{\rho_x g A_x N} \quad (B2)$$

Pressure gradient through stage. - The air pressure in the passage between the blades is determined assuming a reversible adiabatic-state change expressed in terms of the initial state and velocity at the blade section.

$$p_x = p_c \left( 1 + \frac{V_c^2 - V_x^2}{2gRT_c \frac{\gamma}{\gamma-1}} \right)^{\frac{\gamma}{\gamma-1}} \quad (B3)$$

The velocity  $V_x$  as determined from equation (B2) is a function of density  $\rho_x$  and area  $A_x$ . Inasmuch as  $\rho_x$  is a function of  $p_x$ , solution of equations (B2) and (B3) would involve extensive computation. In order to simplify the work,  $\rho_x$  was therefore assumed equal to  $\rho_c$ .

Surface temperature in dry air. - Hardy (reference 10) has indicated that in clear air flow the temperature of the unheated surface for laminar flow will equal

$$t_{s\ x} = t_c + \frac{V_c^2}{2gJc_p} \left[ 1 - \frac{V_x^2}{V_c^2} \left( 1 - \text{Pr}^{\frac{1}{2}} \right) \right] \quad (B4)$$

and for turbulent flow will equal

$$t_{s\ x} = t_c + \frac{V_c^2}{2gJc_p} \left[ 1 - \frac{V_x^2}{V_c^2} \left( 1 - \text{Pr}^{\frac{1}{3}} \right) \right] \quad (B5)$$

The index of  $Pr$  is dependent upon the type of flow, laminar or turbulent; for the conditions of icing used in this analysis a Prandtl number of 0.72 was assumed.

Unit thermal conductance. - Three values of unit thermal conductance taken from reference 11 were considered in this analysis - those for stagnation, laminar, and turbulent flow.

Stagnation:

$$h_x = 0.194 T_{av}^{0.49} \left( \frac{V_c g \rho_c}{D} \right)^{0.5} \quad (B6)$$

Laminar flow:

$$h_x = 0.0562 T_{av}^{0.5} \left( \frac{V_x g \rho_c}{s} \right)^{0.5} \quad (B7)$$

Turbulent flow:

$$h_x = 0.524 T_{av}^{0.296} \left( \frac{V_x g \rho_c}{s^{0.25}} \right)^{0.8} \quad (B8)$$

The temperature  $T_{av}$  is the average of inlet-air temperature and blade-surface temperature.

The location of the point of transition from laminar to turbulent flow is important because of its effect on the heat-transfer coefficient. Because there is no reliable method of determining this point with the presence of water on the surface, however, a location of 10-percent chord was selected.

Local vapor pressures. - The assumption is made that the air is initially of high humidity and, because of a rapid change in pressure as the air passes over the vanes, there is little or no change in state except that the air becomes supersaturated. The local vapor pressure will then be

$$e_x = e_c \frac{P_x}{P_c} \quad (B9)$$

Heat required. - The heat dissipation from a surface in conditions of icing may be divided into its four components:

- (1) Dissipation of heat due to convection from the surface to the air
- (2) Dissipation of heat by evaporation of water from surface because of difference in vapor pressure
- (3) Dissipation of heat as a result of raising temperature of impinging water
- (4) Dissipation of heat due to radiation from relatively warmer surface

For this analysis, the convex surface of the blade was assumed to dissipate heat only by convection and evaporation, because very little, if any, water is assumed to impinge upon the convex surface of the blade. Heat losses due to radiation were small and were neglected.

Dissipation of heat due to convection and evaporation. - The heat dissipated as a result of convection and evaporation was computed by the following simplified equation, as derived from reference 10:

$$H_1 + H_2 = h_x \left[ (t_s - t_{s_x}) + \frac{0.622 L}{c_p} \left( \frac{e_s - e_x}{p_x} \right) \right] \quad (B10)$$

Water impingement. - The water impingement per unit area of leading edge and vane surface was computed assuming a collection efficiency of 100 percent. The areas affected were evaluated from the geometry of the guide vane with straight-line impingement assumed on all exposed surfaces.

The average water impingement per unit area of leading edge was calculated as follows:

$$M_e = \frac{2}{\pi} V_c m (3600) \quad (B11)$$

The water impingement per unit area of vane surface was calculated by the following equation, which represents the concave surface as a plane surface parallel to the chord line:

$$M_s = 3600 \text{ m } V_c \sin \alpha \quad (\text{B12})$$

Dissipation of heat as result of raising temperature of impinging water. - At the leading edge and for the concave blade surface, the rate of heat dissipation was computed with the assumed collection efficiency. The heat required to raise the temperature of the impinging water to that of the blade was therefore equal to

$$H_3 = Mc_{pw} (t_s - t_c) \quad (\text{B13})$$

neglecting the small kinetic temperature rise in the impinging water.

Total heat dissipation. - The total heat dissipation for the leading edge and the concave blade surface is the summation of the three types of heat loss

$$H = (H_1 + H_2) + H_3 \quad (\text{B14})$$

whereas the total heat dissipation of the convex blade surface was assumed to be

$$H = H_1 + H_2 \quad (\text{B15})$$

The average heat dissipation presented per square foot of vane surface (fig. 18(a)) is the integrated average of the dissipation rates for both sides of the vane. The heat dissipation due to evaporation,  $H_2$  in equation (B15), is assumed to apply because some moisture will probably run back on the convex face. Also, the heat requirement for the convex face must be nearly as high as that for the concave face to prevent the development of regions of subfreezing temperatures on the blades. The increase in heating requirement that results from this conservative assumption should help to safeguard the leading edge by action of conduction in the blade metal.

#### REFERENCES

1. von Glahn, Uwe: Ice Protection of Turbojet Engines by Inertia Separation of Water. I - Alternate-Duct System. NACA RM E8A27, 1948.
2. Fleming, William A., and Saari, Martin J.: Inlet Icing and Effectiveness of Hot-Gas Bleedback for Ice Protection of Turbojet Engine. NACA RM E8J25c, 1948.



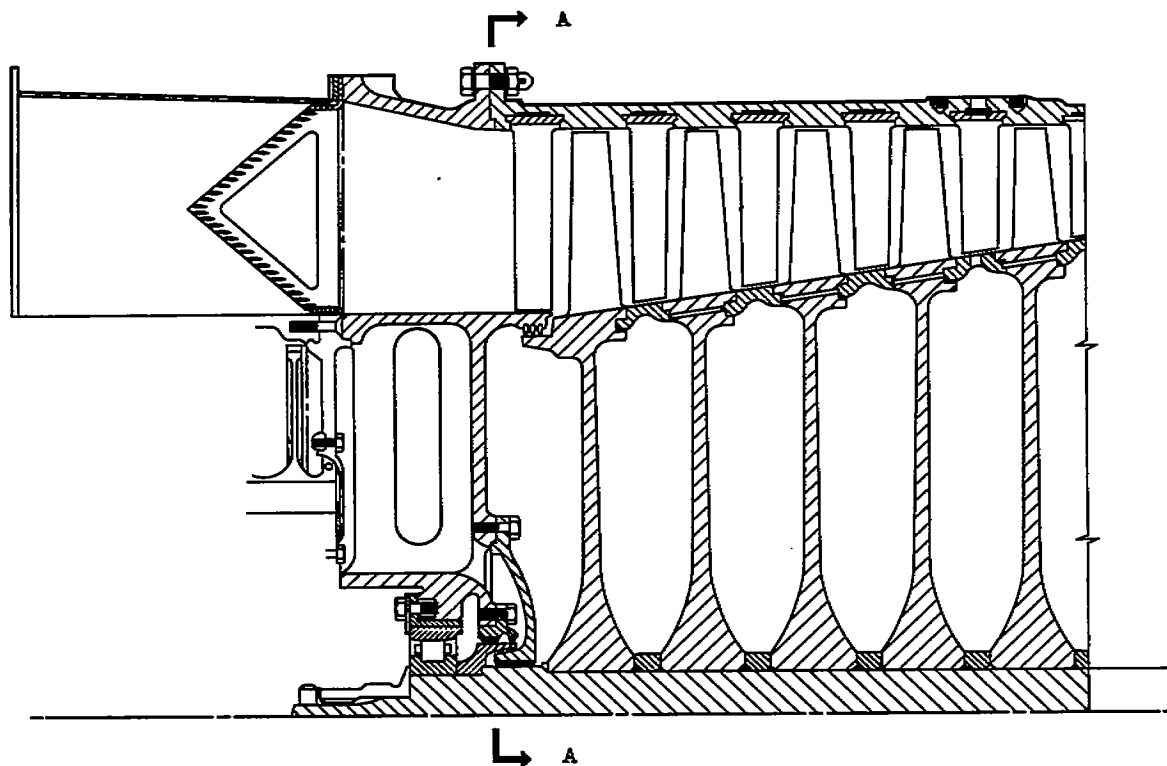
3. Gray, V. H., and Campbell, R. G.: A Method for Estimating Heat Requirements for Ice Prevention on Gas-Heated Hollow Propeller Blades. NACA TN 1494, 1947.
4. Steinmetz, Charles Proteus: Theory and Calculation of Transient Electric Phenomena and Oscillations. McGraw-Hill Book Co., Inc., 3d ed., 1920, pp. 361-374.
5. Anon.: Electrical Steel Sheets. Bull. No. 2, Carnegie-Illinois Steel Corp. (Pittsburgh, Pa.), 1941, p. 112.
6. Roters, Herbert C.: Electromagnetic Devices. John Wiley & Sons, Inc., 1941, pp. 116-150.
7. Anon.: Armco Magnetic Ingot Iron. The American Rolling Mill Co. (Middletown, Ohio), 1945.
8. Anon.: Westinghouse Metals and Alloys for Communications and Electronics Equipment. Westinghouse Electric Corp. (East Pittsburgh, Pa.).
9. Lewis, William: A Flight Investigation of the Meteorological Conditions Conducive to the Formation of Ice on Airplanes. NACA TN 1393, 1947.
10. Hardy, J. K.: Protection of Aircraft against Ice. Rep. No. S.M.E.3380, British R.A.E., July 1946.
11. Martinelli, R. C., Guibert, A. G., Morrin, E. H., and Boelter, R. M. K.; An Investigation of Aircraft Heaters. VIII - A Simplified Method for the Calculation of the Unit over Wings. NACA ARR, March 1943.

TABLE I - SUMMARY OF PERTINENT VALUES

1	2	3	4	5	6	7	8	9	10	11	12	13	14	15
$H_{\max 2}$ (oer- stedts)	$H_{\max 1}$ (oer- stedts)	$\alpha_2$ (deg)	$\beta_2 - \delta_2$ (deg)	$P_T$ (cm)	$l_T$ (cm)	$N_R I_{\max a}$	$N_D I_{\max b}$	NI	$E_2$ (volts/ cm)	Measured $E_2$ (volts/ cm)	$p_e'$ (watts/ sq in.)	Measured $p_e'$ (watts/ sq in.)	$\mu$	$c$ (1/cm)
SAE 1020 steel, measured $\gamma = 0.594 \times 10^5$ mho/cm														
6	4.31	0.60	1.30	8.60	0.0049	16.8	56.1	51.6	0.0140	0.0127	0.22	0.25	2665	195.5
30	5.63	4.25	8.62	9.01	.0123	37.2	280.5	224.7	.0379	.0400	3.33	3.50	2665	195.5
50	5.93	5.26	9.82	9.24	.0163	46.7	468.0	364.0	.0502	.0535	7.44	7.60	2665	195.5
Armco Magnetic Ingot Iron, measured $\gamma = 0.873 \times 10^5$ mho/cm														
6	2.83	1.65	3.90	8.56	0.0043	14.7	56.1	50.0	0.0128	0.0115	0.21	0.21	4590	311
30	3.49	5.30	9.88	8.90	.0104	31.1	280.5	220.2	.0325	.0350	2.87	2.80	4590	311
50	3.60	6.05	10.10	9.10	.0138	40.0	468.0	359.0	.0426	.0444	6.34	6.70	4590	311
Hipernik, measured $\gamma = 0.248 \times 10^5$ mho/cm														
6	0.256	6.68	10.15	8.66	0.0104	23.7	56.1	56.4	0.0241	0.0240	0.43	0.40	50,000	546
20	.280	7.55	10.25	9.13	.0190	42.6	187.0	162.3	.0458	.0510	2.74	2.50	50,000	546
40	.300	7.88	10.30	9.54	.0264	59.3	374.0	306.5	.0667	.0780	7.96	8.40	50,000	546

NACA





Section A-A



NACA  
C-21056  
4-1-48

Figure 1. - Axial-flow compressor with front view of inlet guide vanes.



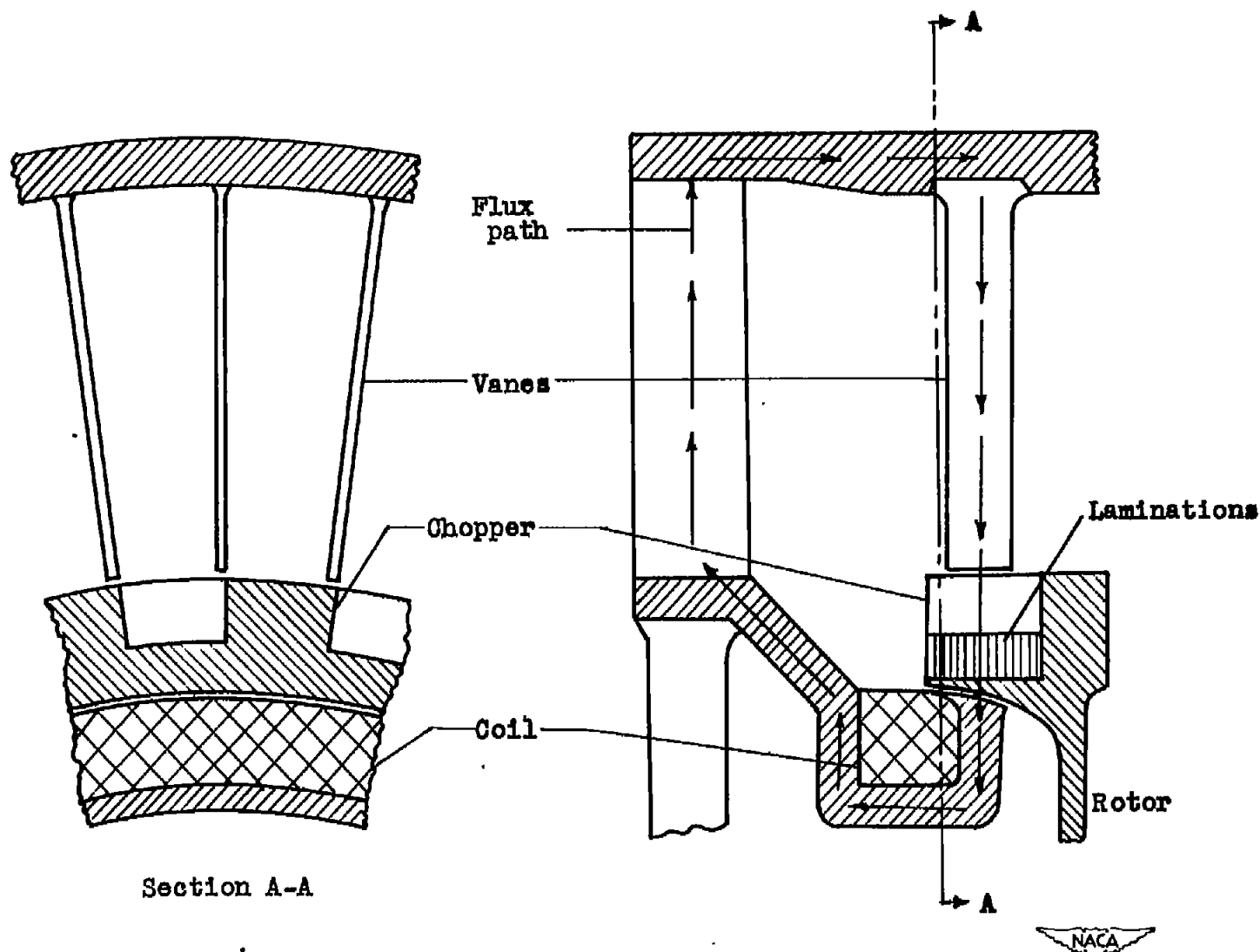


Figure 2. - Schematic diagram illustrating principle of eddy-current heating applied to inlet guide vanes of axial-flow compressor.

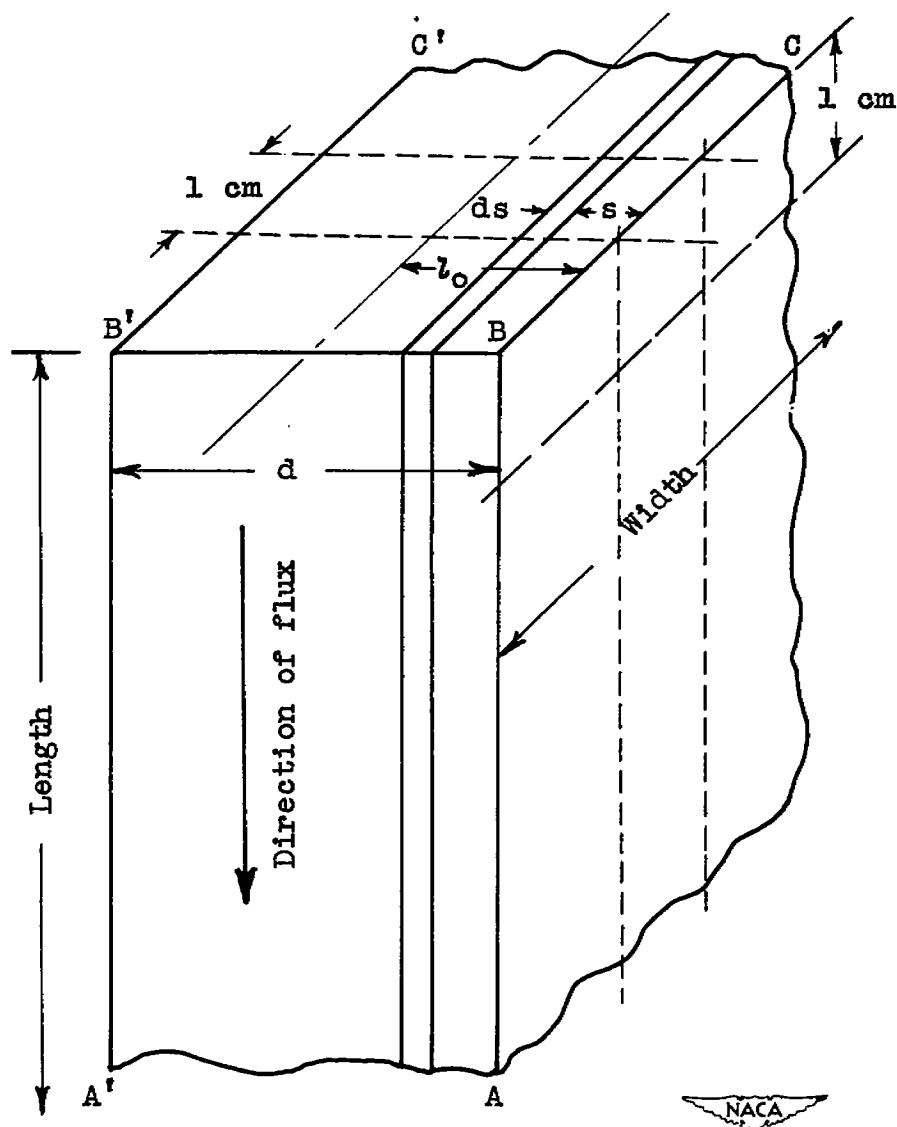


Figure 3. - Section of plate.

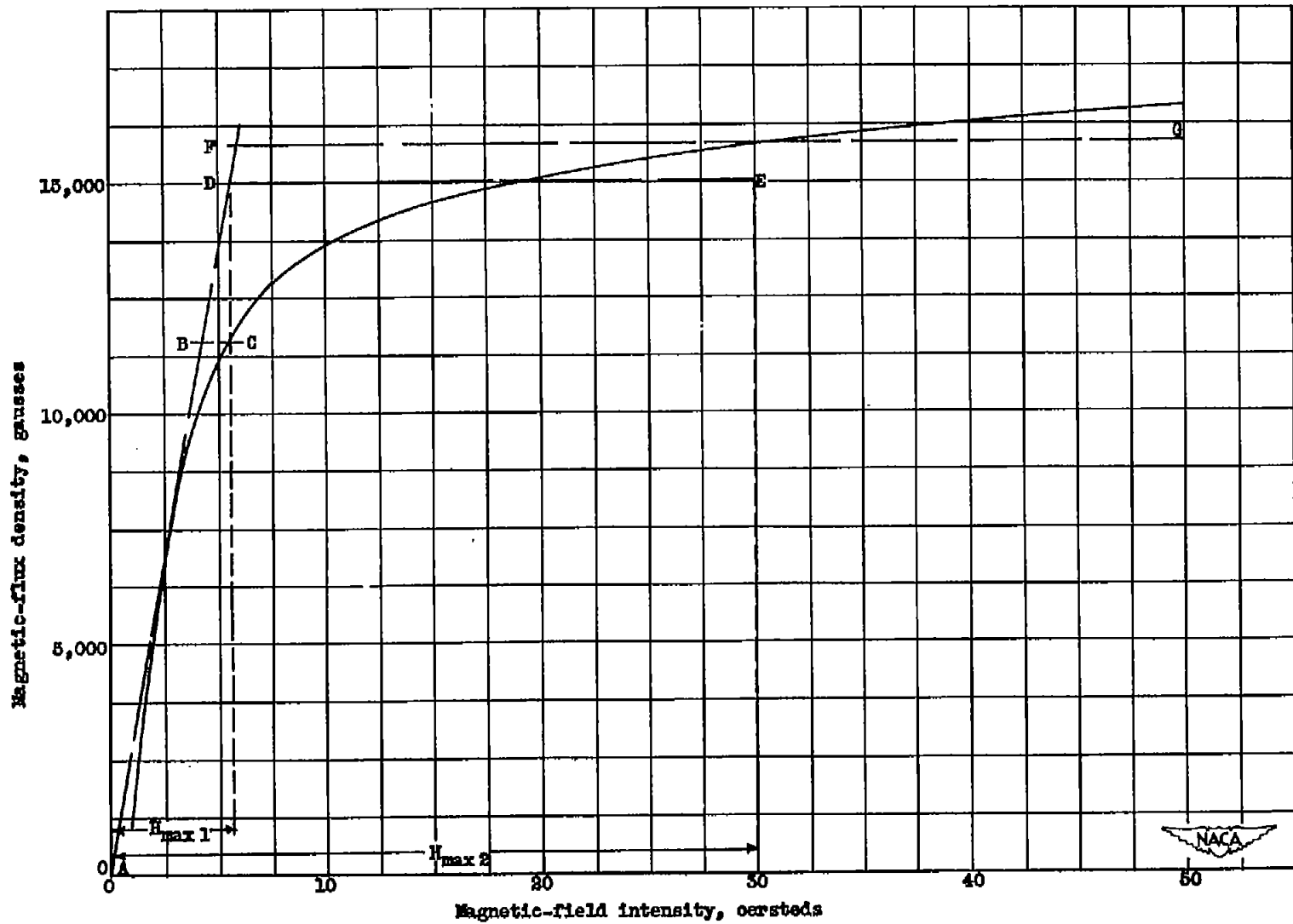


Figure 4. - Normal magnetisation curve for SAE 1020 steel annealed at 1500° F and furnace-cooled.  
(Data from reference 5.)



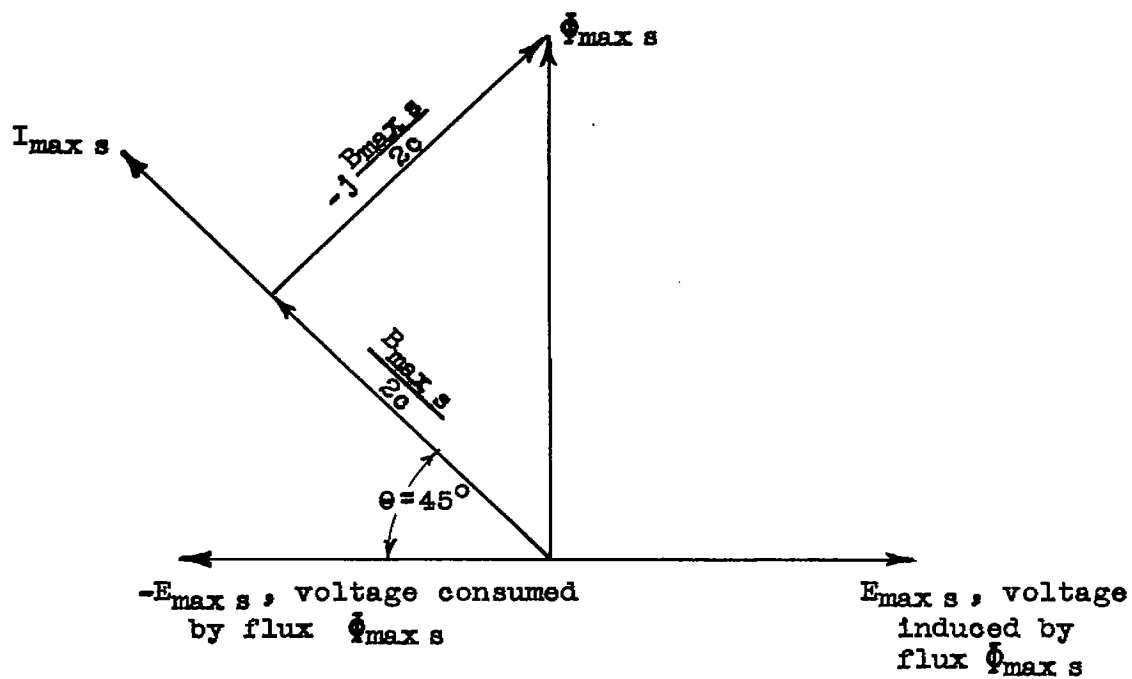


Figure 5. - Vector diagram of phase relation of current, flux, and voltage at constant permeability.

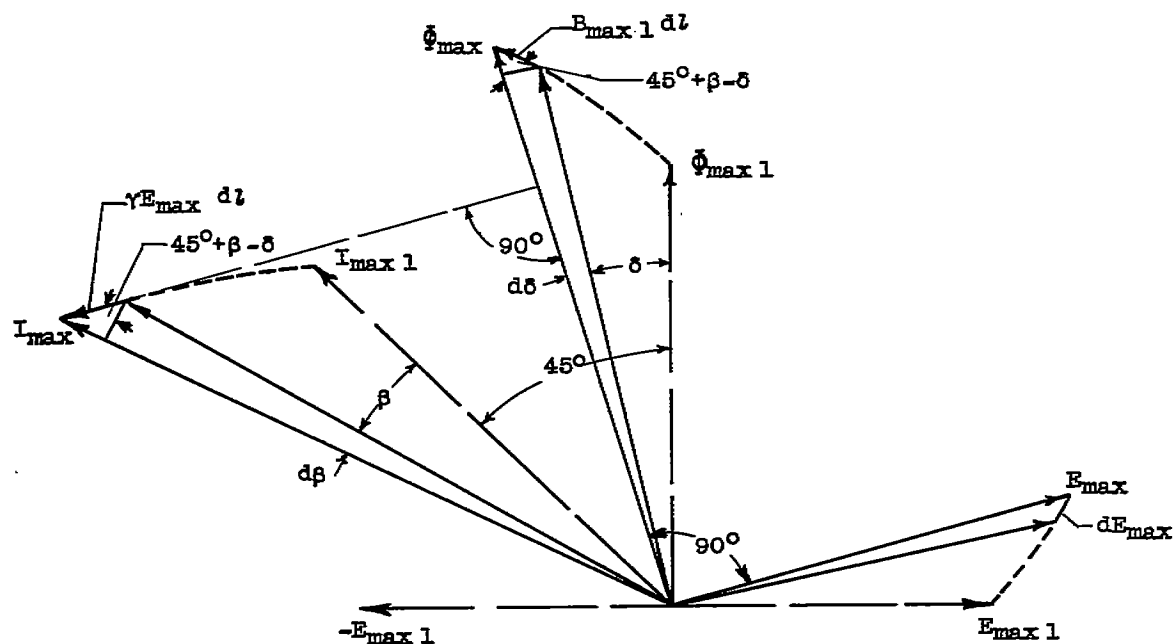
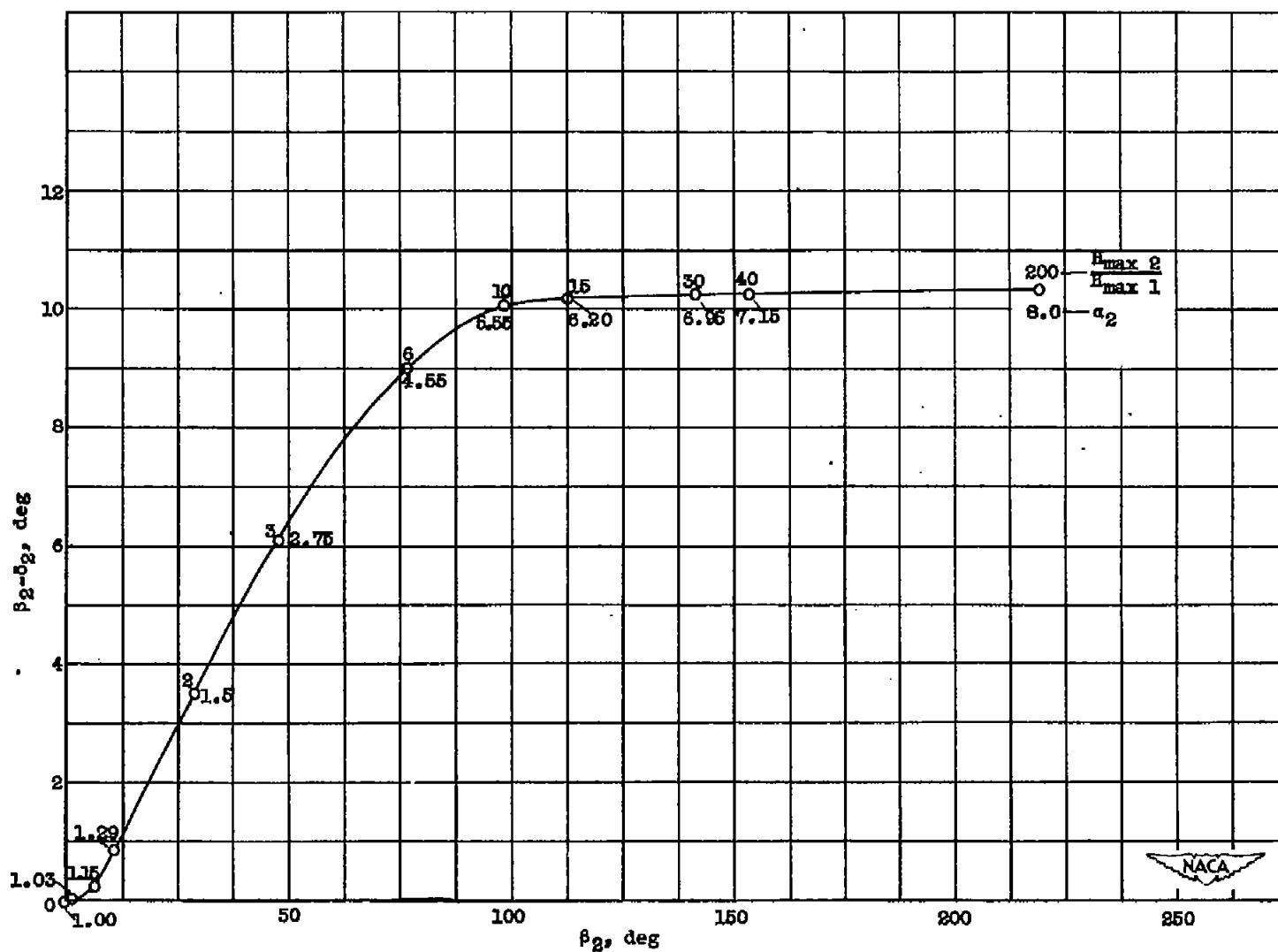


Figure 6. - Vector diagram of phase relation of current, flux, and voltage under conditions of saturation.

Figure 7. - Variation of  $\beta_2 - \delta_2$  with  $\beta_2$ .

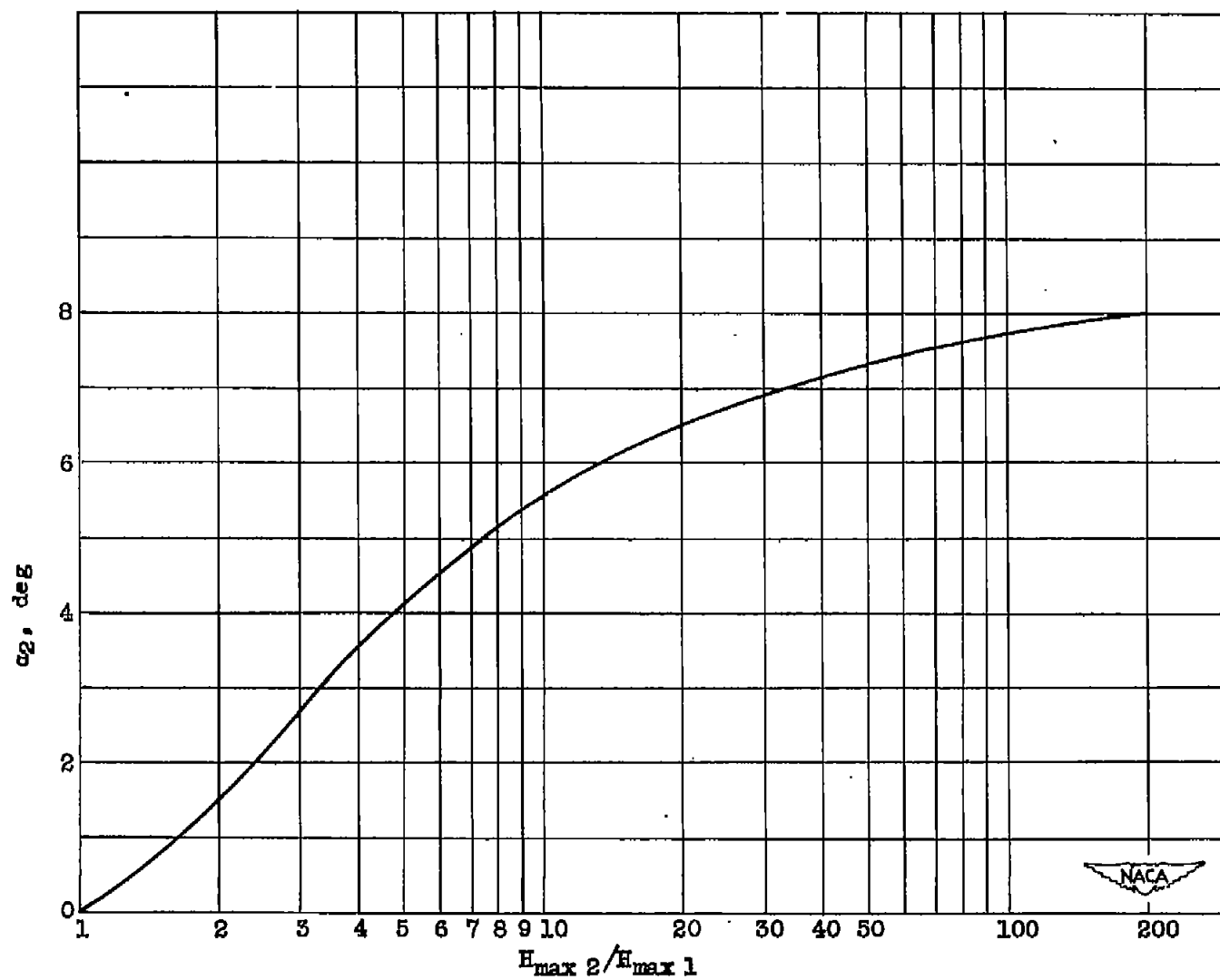


Figure 8. - Variation of  $\alpha_2$  with  $H_{\max 2} / H_{\max 1}$ .

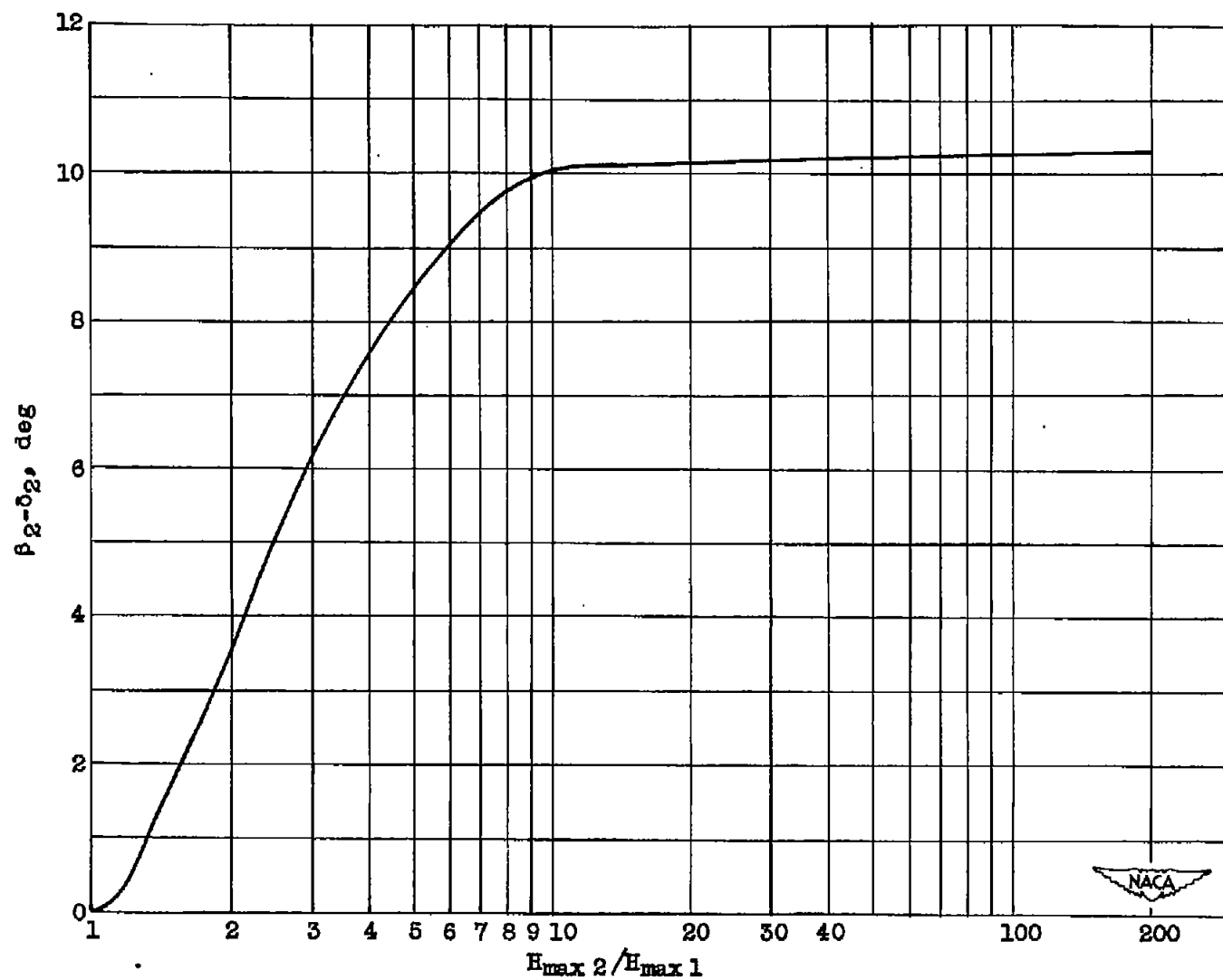


Figure 9. - Variation of  $\beta_2 - \delta_2$  with  $H_{\max 2} / H_{\max 1}$ .

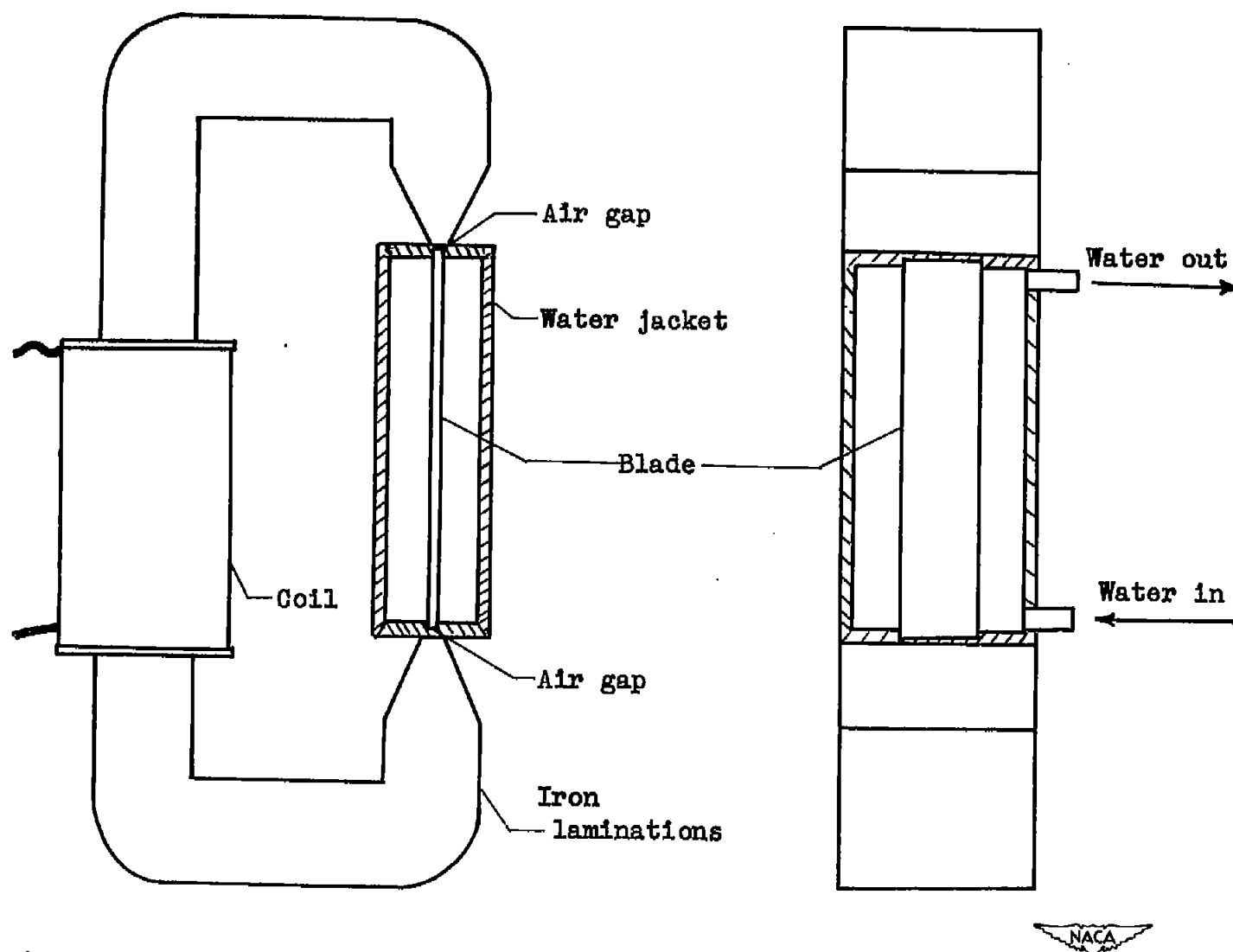


Figure 10. - Equipment utilized for determining eddy-current heat generated in blade.

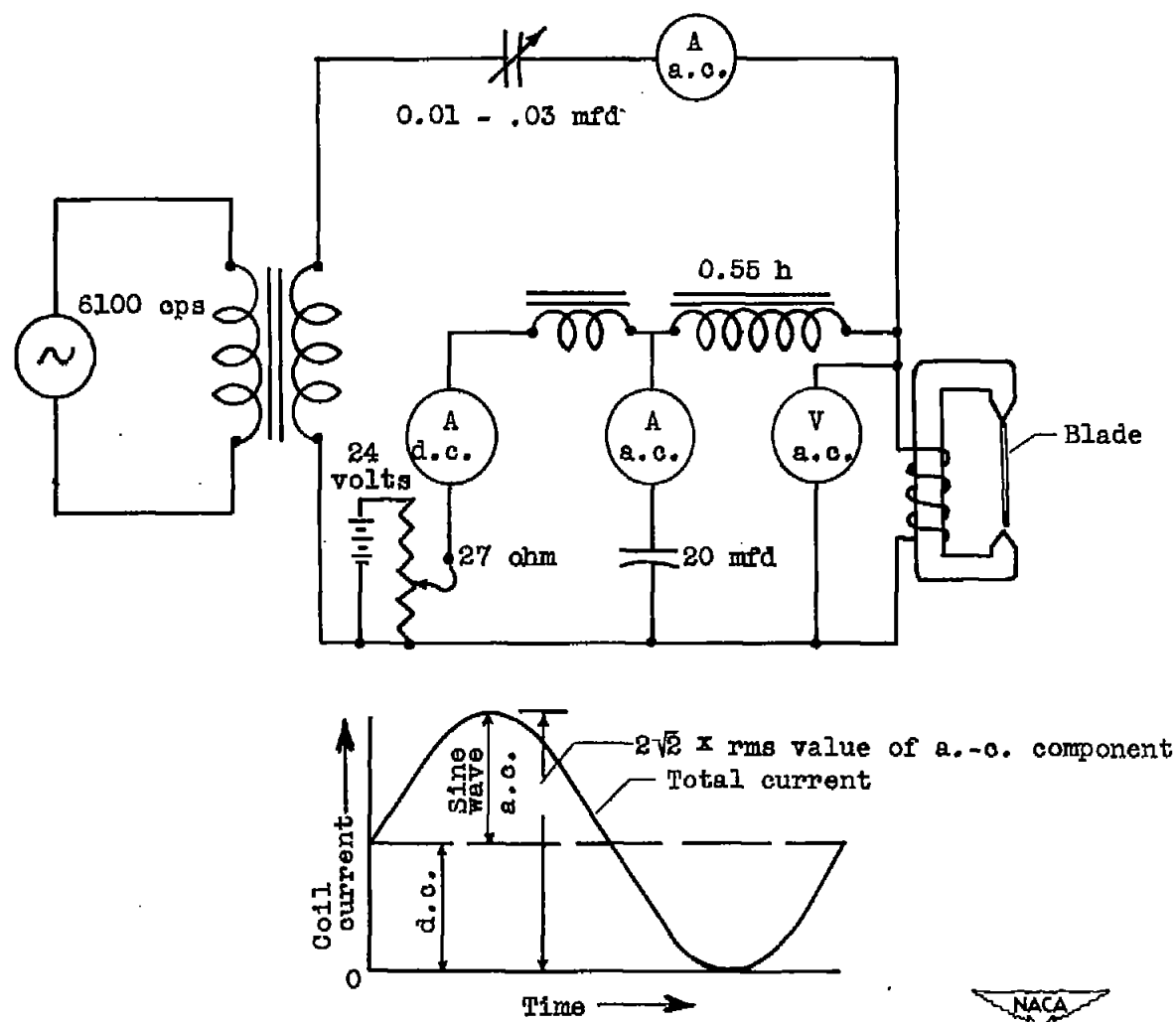


Figure 11. - Circuit schematic diagram for alternating-current plus direct-current experiment.

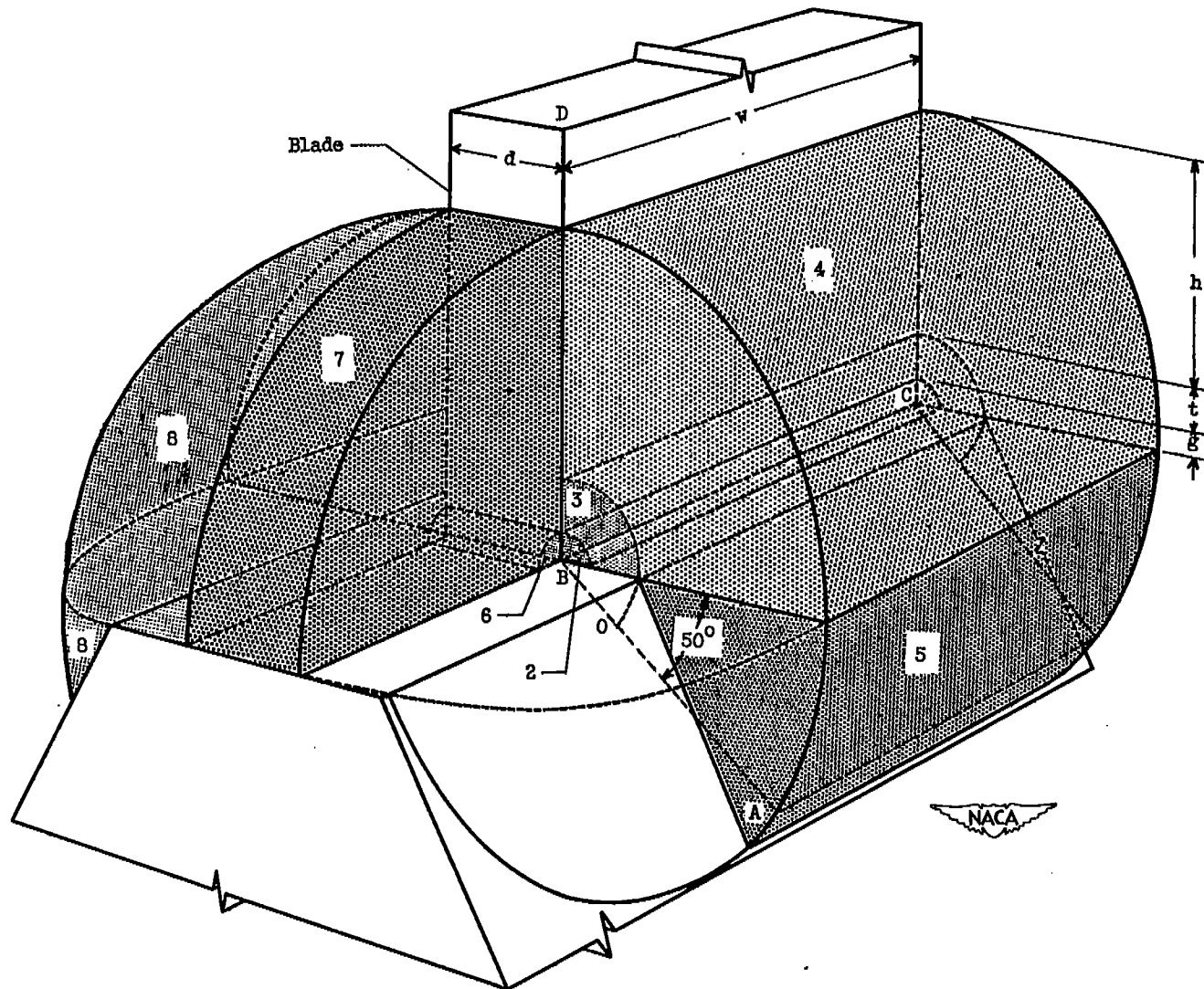


Figure 12. - Geometry used in permeance calculations.



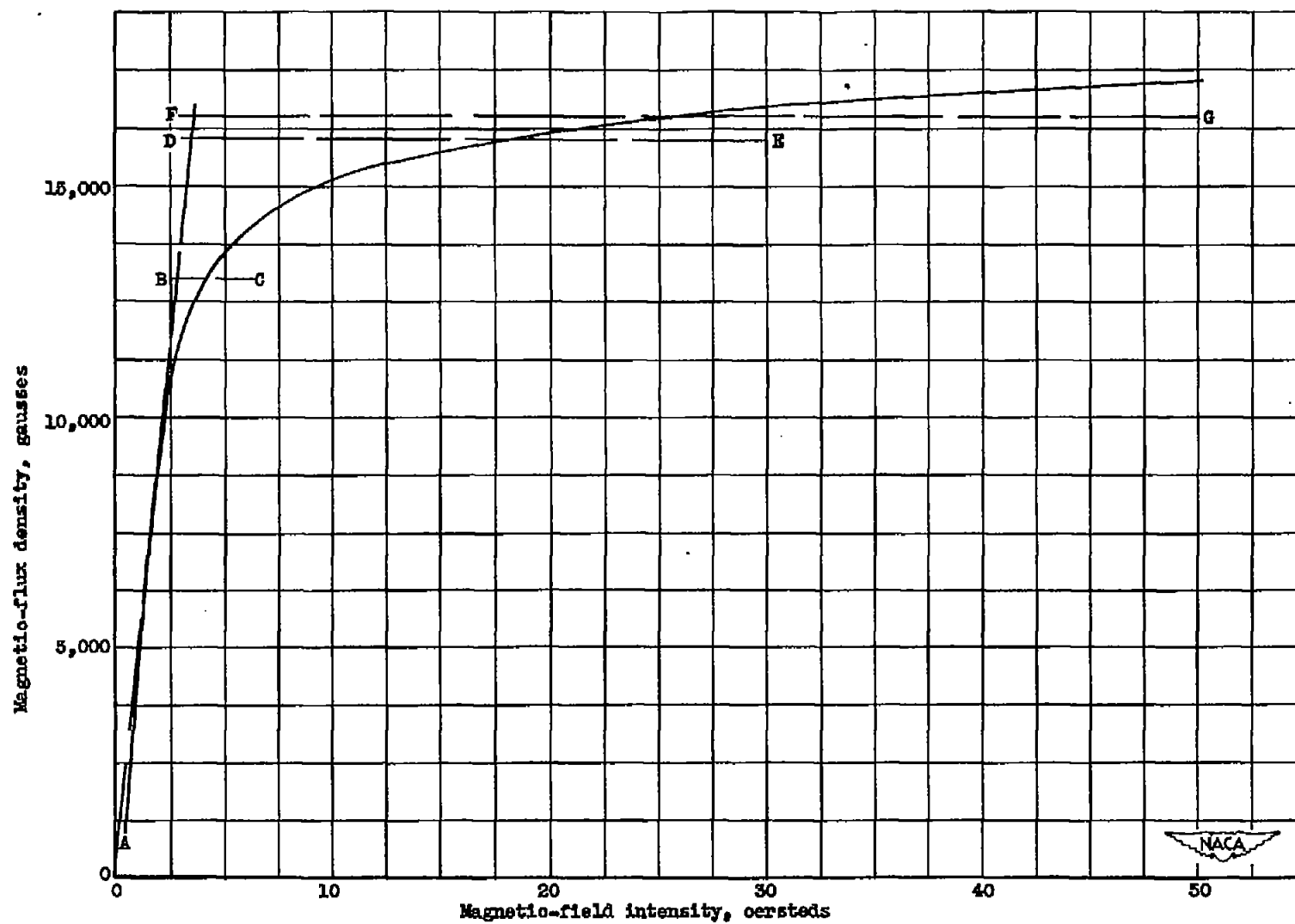


Figure 13. - Normal magnetization curve for Armo Magnetic Ingot Iron.  
(Data from reference 7.)

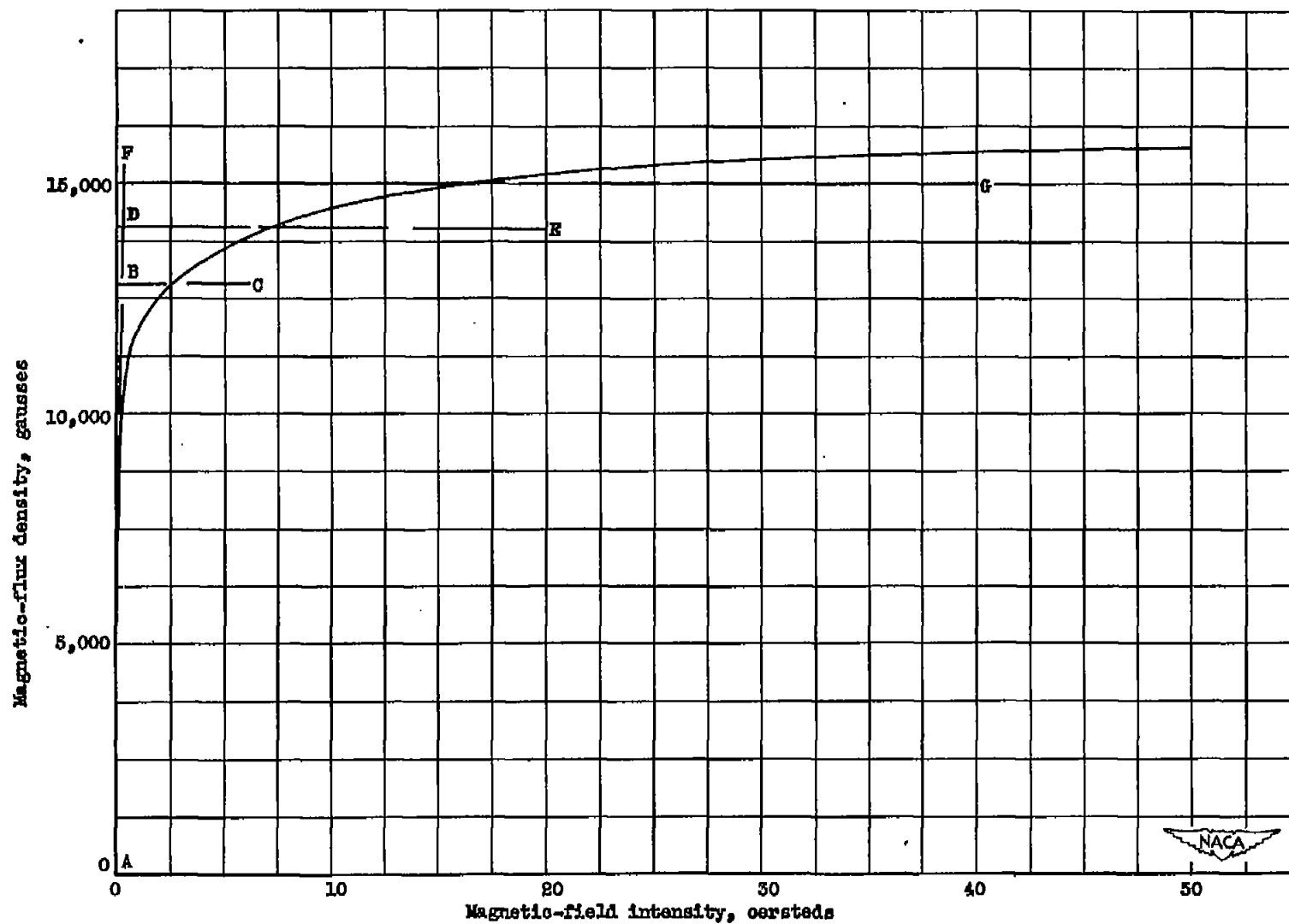


Figure 14. - Magnetization curve for Hipernik.  
(Data from reference 8.)

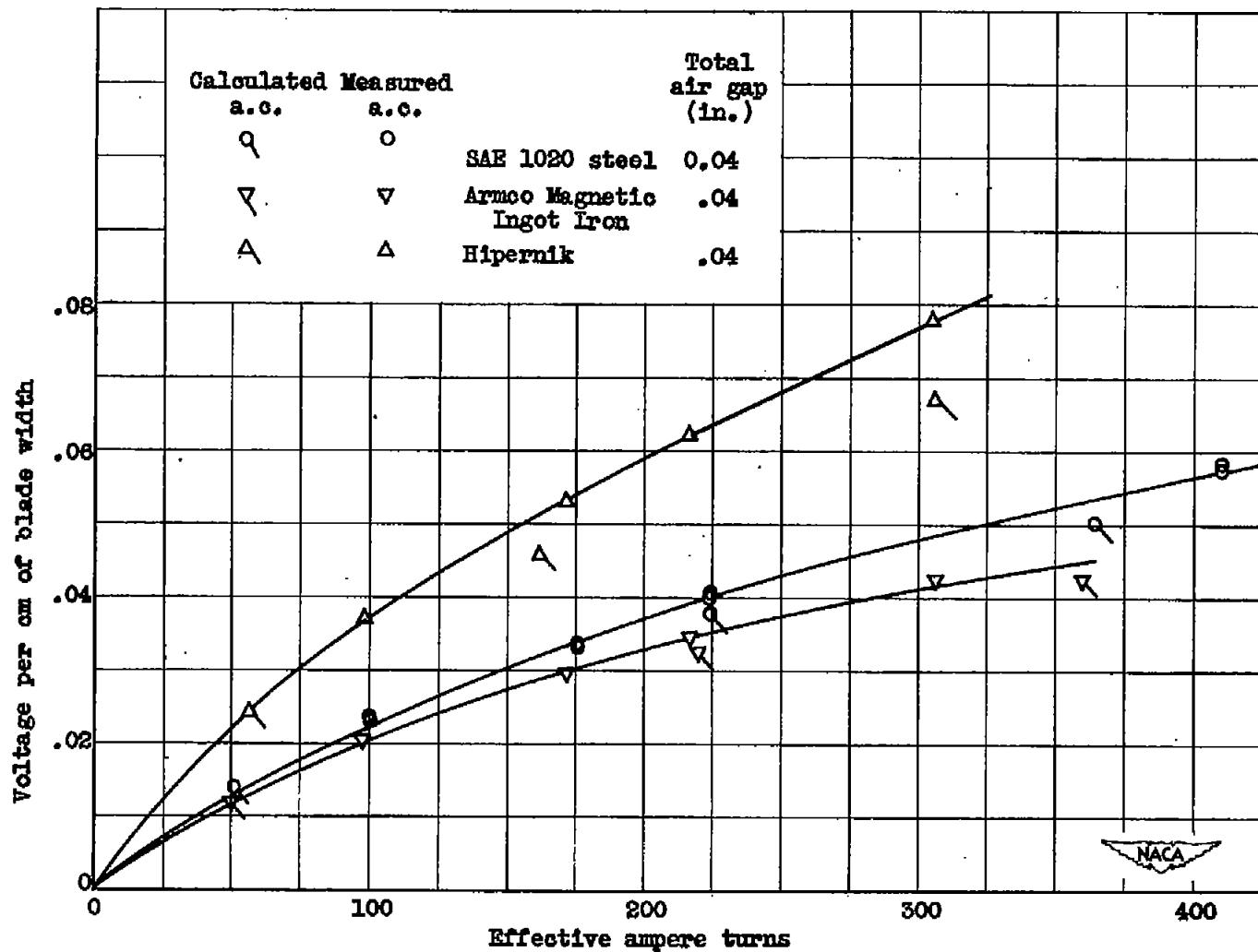


Figure 15. - Variation of voltage of self-induction per centimeter of blade width with ampere turns. Vane,  $4\frac{5}{8}$  by 1 by  $\frac{1}{8}$  inch (Hipernik,  $4\frac{5}{8}$  by 1 by 0.094 in.); frequency, 6100 cycles per second.

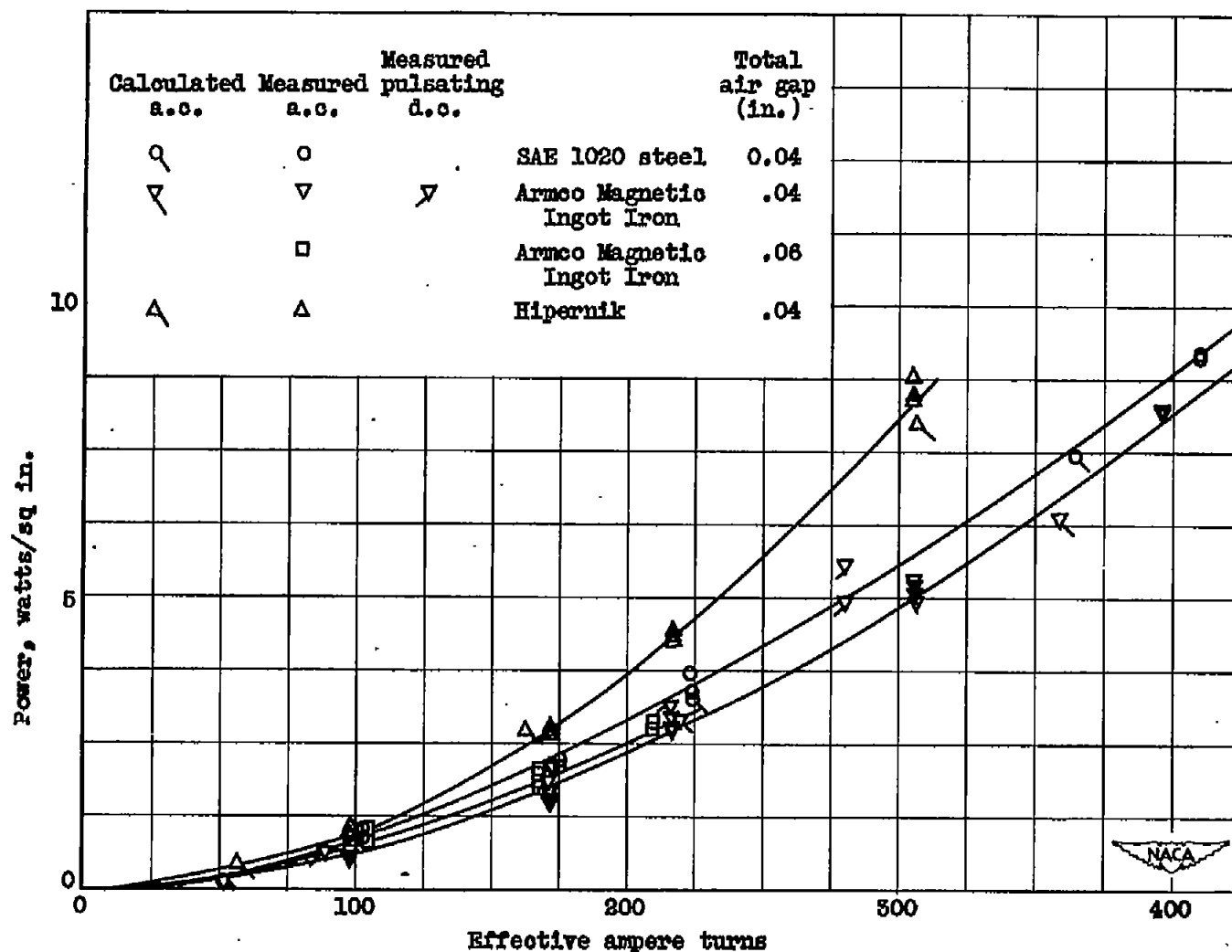


Figure 16. - Ampere turns required for eddy-current heating. Vane,  $4\frac{5}{8}$  by 1 by  $\frac{1}{8}$  inch (Hipernik,  $4\frac{5}{8}$  by 1 by 0.094 in.); frequency, 6100 cycles per second.

•

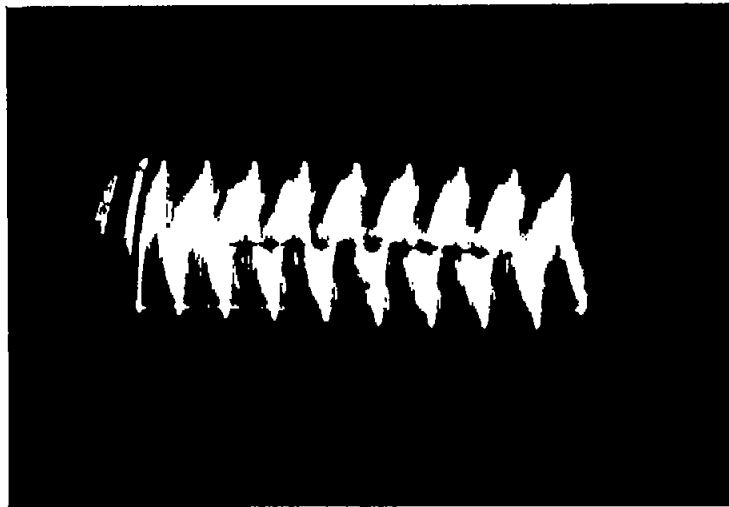
•

•

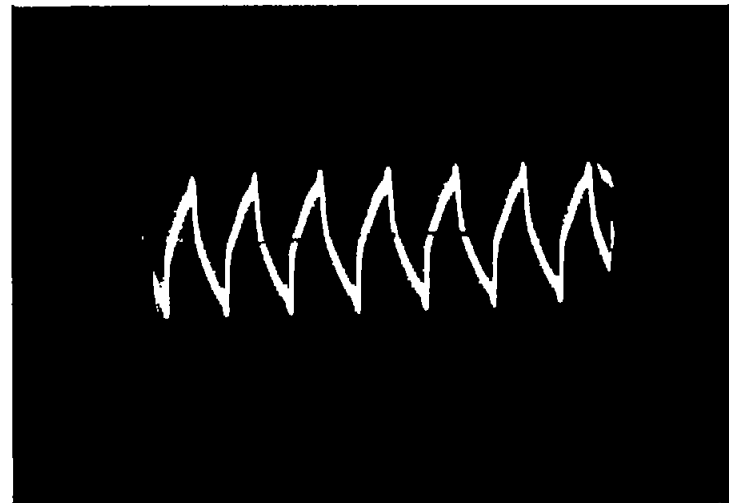
•

•

•



(a) 99 root-mean-square ampere turns.



(b) 89 root-mean-square ampere turns; 139 direct-current ampere turns.

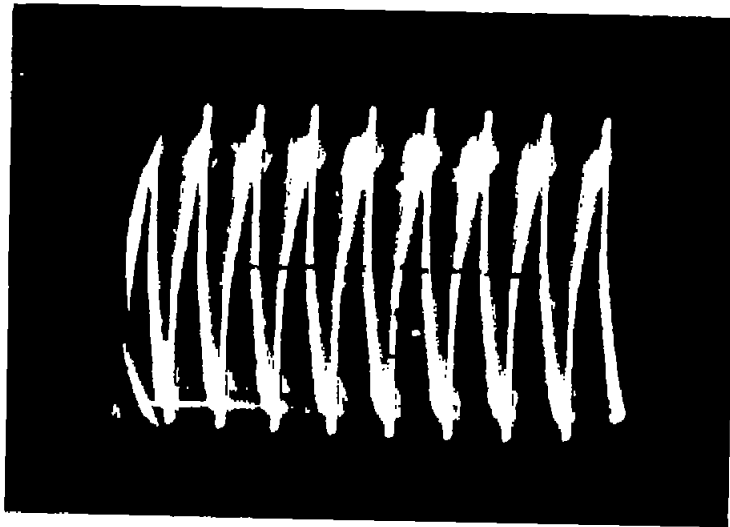


C-23405

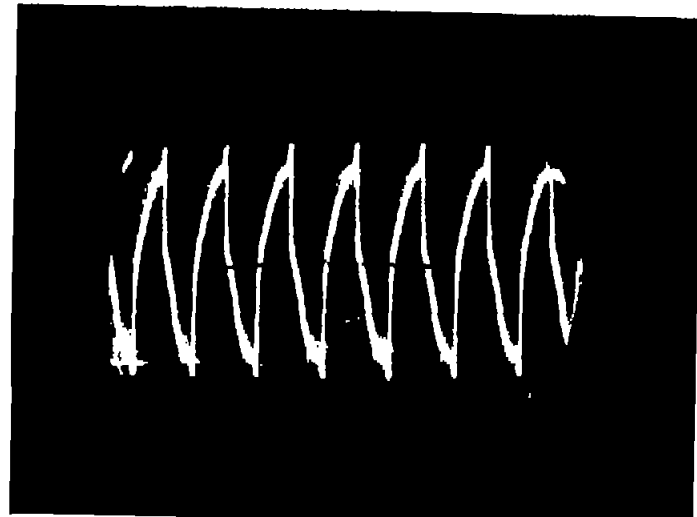
5-8-48

Figure 17. - Search-coil voltage oscillograms for comparing wave shapes with and without superimposed direct-current ampere turns. Armco Magnetic Ingot Iron; air gap, 0.04 inch.





(c) 383 root-mean-square ampere turns.



(d) 281 root-mean-square ampere turns; 414 direct-current ampere turns.



C-23406  
5-5-49

Figure 17. - Concluded. Search-coil voltage oscillograms for comparing wave shapes with and without superimposed direct-current ampere turns. Armo Magnetic Ingot Iron; air gap, 0.04 inch.





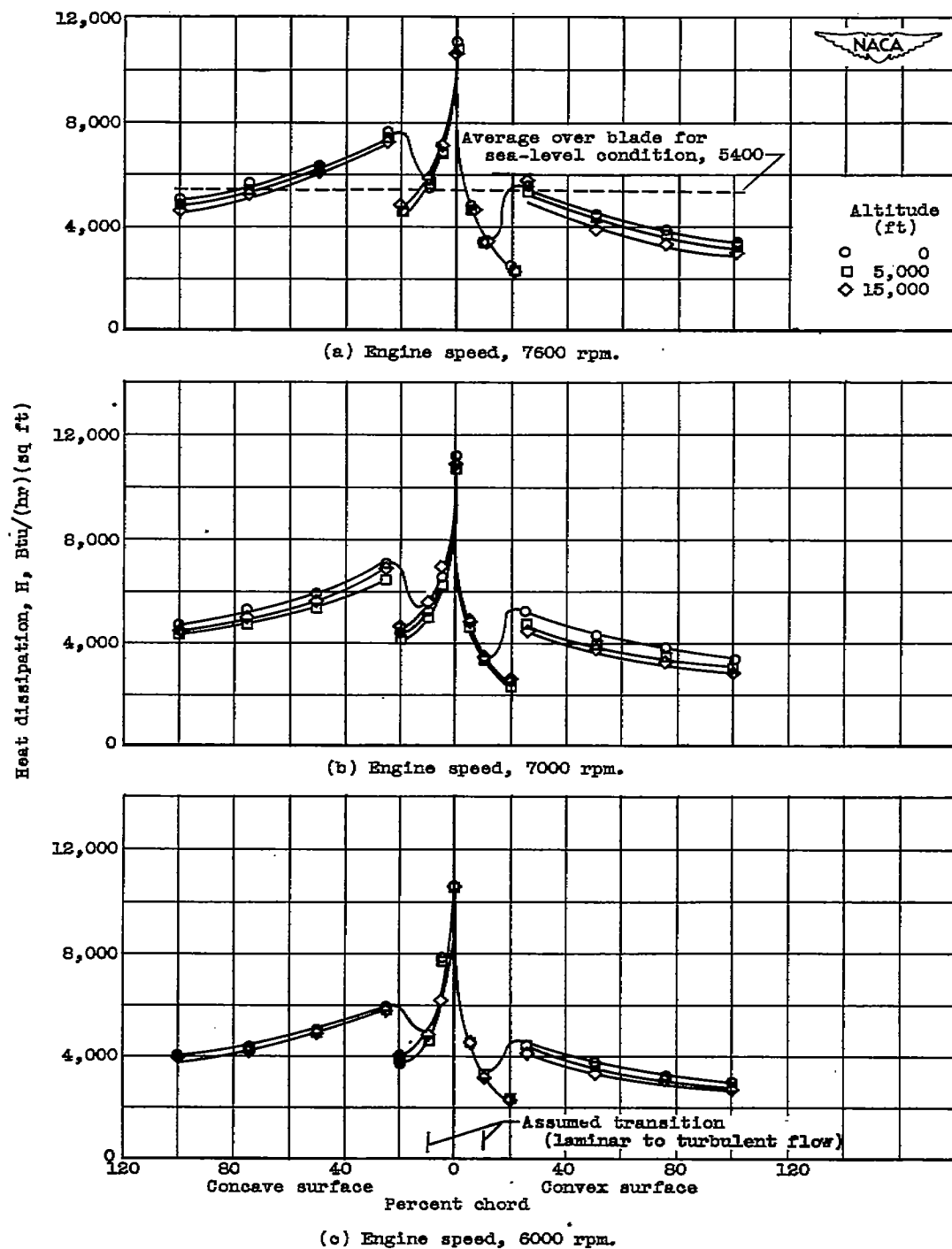


Figure 18. - Calculated unit heat dissipation along inlet-guide-vane chord in icing condition. Blade-surface temperature,  $35^{\circ}\text{F}$ ; inlet-air temperature,  $0^{\circ}\text{F}$ ; liquid-water content, 1 gram per cubic meter.

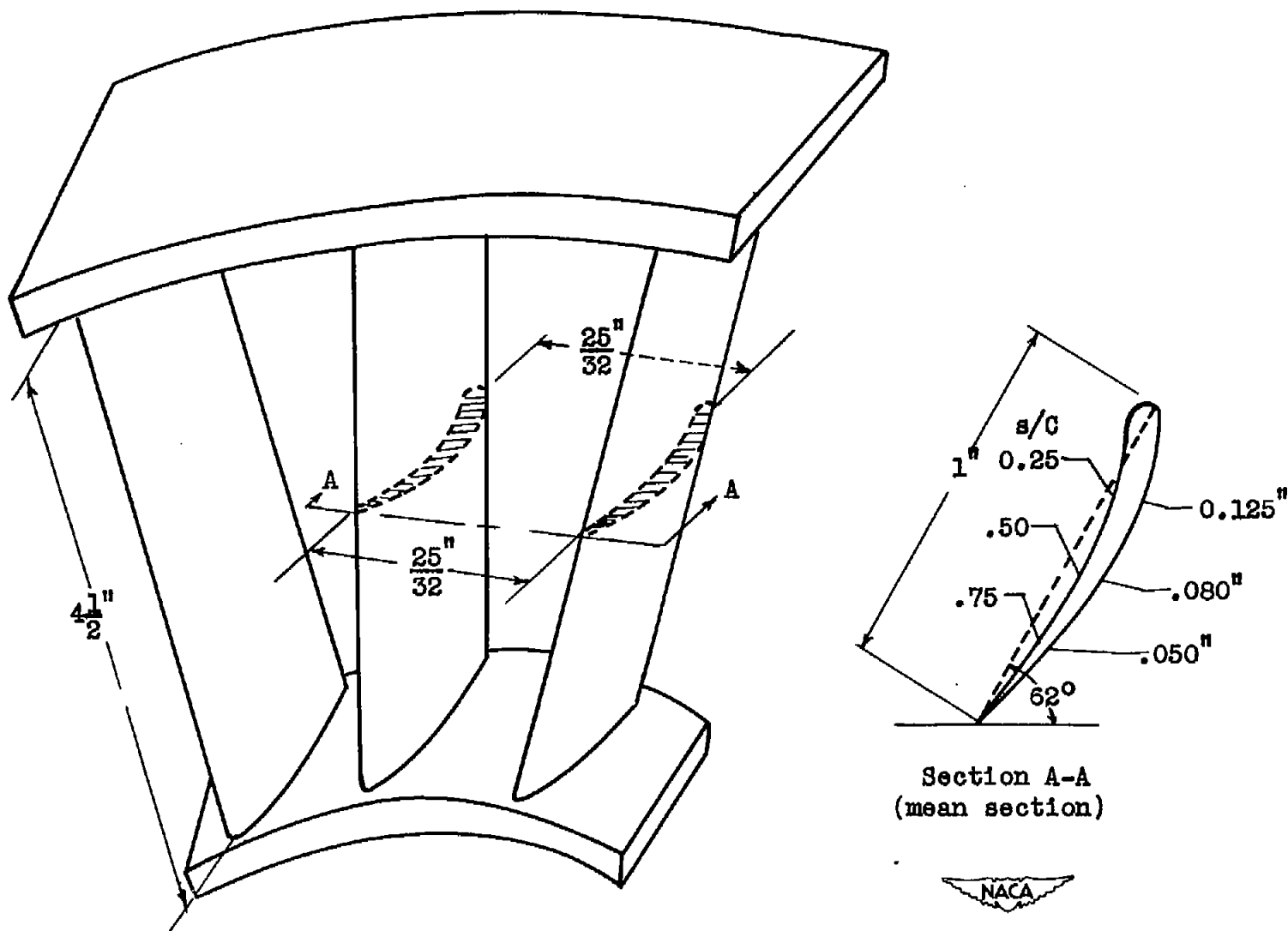
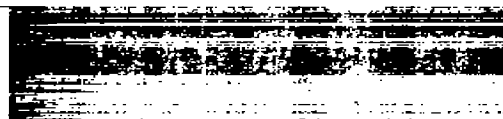


Figure 19. - Physical dimensions of inlet guide vanes of typical axial-flow compressor.

NASA Technical Library



3 1176 01435 0830



1

2

3

4

5

6